

# Dense gas in IRAS 20343+4129: an ultracompact H II region caught in the act of creating a cavity

F. Fontani,<sup>1\*</sup> Aina Palau,<sup>2</sup> G. Busquet,<sup>3</sup> A. Isella,<sup>4</sup> R. Estalella,<sup>5</sup> Á. Sanchez-Monge,<sup>1</sup> P. Caselli<sup>6</sup> and Q. Zhang<sup>7</sup>

<sup>1</sup>INAF-Osservatorio Astrofisico di Arcetri, L.go E. Fermi 5, Firenze I-50125, Italy

<sup>2</sup>Institut de Ciències de l'Espai (CSIC-IEEC), Campus UAB-Facultat de Ciències, Torre C5-parell 2, Bellaterra, E-08193 Catalunya, Spain

<sup>3</sup>INAF-Istituto di Fisica dello Spazio Interplanetario, Via Fosso del Cavaliere 100, Roma I-00133, Italy

<sup>4</sup>Division of Physics, Mathematics and Astronomy, California Institute of Technology, MC 249-17, Pasadena, CA 91125, USA

<sup>5</sup>Departament de Astronomia i Meteorologia (IEEC-UB), Institut de Ciències del Cosmos, Universitat de Barcelona, Martí Franquès 1, E-08028 Barcelona, Spain

<sup>6</sup>School of Physics and Astronomy, University of Leeds, Leeds LS2 9JT

<sup>7</sup>Harvard-Smithsonian Center for Astrophysics, 60 Garden Street MS78, Cambridge, MA 02138, USA

Accepted 2012 March 23. Received 2012 March 23; in original form 2012 January 4

## ABSTRACT

The intermediate- to high-mass star-forming region IRAS 20343+4129 is an excellent laboratory to study the influence of high- and intermediate-mass young stellar objects on nearby starless dense cores, and investigate for possible implications in the clustered star formation process. We present 3 mm observations of continuum and rotational transitions of several molecular species ( $C_2H$ ,  $c-C_3H_2$ ,  $N_2H^+$ ,  $NH_2D$ ) obtained with the Combined Array for Research in Millimetre-wave Astronomy, as well as 1.3 cm continuum and  $NH_3$  observations carried out with the Very Large Array, to reveal the properties of the dense gas. We confirm undoubtedly previous claims of an expanding cavity created by an ultracompact H II region associated with a young B2 zero-age main sequence (ZAMS) star. The dense gas surrounding the cavity is distributed in a filament that seems squeezed in between the cavity and a collimated outflow associated with an intermediate-mass protostar. We have identified 5 mm continuum condensations in the filament. All of them show column densities consistent with potentially being the birthplace of intermediate- to high-mass objects. These cores appear different from those observed in low-mass clustered environments in several observational aspects (kinematics, temperature, chemical gradients), indicating a strong influence of the most massive and evolved members of the protocluster. We suggest a possible scenario in which the B2 ZAMS star driving the cavity has compressed the surrounding gas, perturbed its properties and induced the star formation in its immediate surroundings.

**Key words:** stars: formation – ISM: individual objects: IRAS 20343+4129 – ISM: molecules.

## 1 INTRODUCTION

Most of the stars of all masses in the Galaxy form in rich clusters. Despite this, the details of the clustered star formation process are still poorly understood. Studies of *low-mass protoclusters* have started to unveil similarities and differences between isolated and clustered dense cores (e.g. André et al. 2007; Foster et al. 2009; Friesen et al. 2009). Globally these studies suggest that cluster environment has a relatively smaller influence on the properties of the cores (temperature, mass, velocity dispersion, chemical abundances of early phase molecules) than is typically assumed (Foster

et al. 2009). However, the conclusions described above do not include observations of *high-mass star-forming regions*. Because the phenomena associated with massive star formation have a stronger impact on the environment (massive outflows, UV radiation, expanding H II regions), it is plausible that these energetic phenomena have major effects on the surrounding dense material. The study of such interaction is especially important to quantify the effect of protostellar feedback on the environment and test recent models of high-mass star formation including outflows and radiation from the newly born stars (e.g. Krumholz, Klein & McKee 2011; Hennebelle et al. 2011).

Interferometric observations of dense gas and dust tracers ( $N_2H^+$ , mm continuum,  $NH_3$ ) have revealed the presence of pre-stellar core candidates surrounding ultracompact H II regions

\*E-mail: fontani@arcetri.astro.it

(UC H II)s and other massive young stellar objects (YSOs) that do show evidence of such an interaction. For example, Fontani et al. (2009) found that in the protocluster associated with IRAS 05345+3157 the kinematics of two pre-stellar core candidates is influenced by the passage of a massive outflow. UV radiation and powerful outflows affect the chemistry of starless cores in IRAS 20293+3952 (Palau et al. 2007a). On the other hand, a crucial chemical process in pre-stellar cores, i.e. the deuteration of species like  $\text{N}_2\text{H}^+$  and  $\text{NH}_3$ , seems to remain as high as in pre-stellar cores isolated and associated with low-mass star-forming regions (Fontani et al. 2008; Busquet et al. 2010; Pillai et al. 2011). Therefore, to date it is not clear if and how the presence of massive objects affects the properties and evolution of the other (pre-)protocluster members.

The protocluster associated with IRAS 20343+4129 (hereafter I20343) represents an excellent laboratory to study this issue. The *IRAS* source is located to the northeastern side of the Cygnus OB2 association, at 1.4 kpc of distance from the Sun (Sridharan et al. 2002; Rygl et al. 2011), and two bright nebulous stars, IRS 1 (north) and IRS 3 (south), are found inside the *IRAS* error ellipse when observed at high angular resolution (Kumar, Bachiller & Davis 2002). The bright infrared stars are embedded in a cometary-like cloud whose head, facing the Cygnus OB2 association, is bright at centimetre wavelengths and whose tail, bright in the mid-infrared, is extending for about 10 arcmin ( $\sim 4$  pc) towards the north-east (Fig. 1). This kind of clouds is also known as bright rimmed clouds.

Thanks to interferometric observations of  $^{12}\text{CO}$  and 1.3 mm continuum, Palau et al. (2007b) concluded that IRS 1 is an intermediate-mass Class I YSO driving a molecular outflow in the east–west direction, while IRS 3 is likely a more evolved intermediate/high-mass star. This is further confirmed through mid-infrared photometric and spectroscopic observations, from which Campbell et al. (2008) also estimated a bolometric luminosity of the order of  $1000 L_\odot$  for both IRS 1 and IRS 3. Furthermore, IRS 3 is at the centre of an UC H II-region detected through Very Large Array (VLA) centime-

tre continuum emission (Carral et al. 1999), and of a fan-shaped emission in the  $2.12 \mu\text{m}$  rovibrational line of molecular hydrogen (Kumar et al. 2002). East and west of this fan-shaped feature, Palau et al. (2007b) detected molecular gas and dust resolved into several millimetre continuum compact sources. Palau et al. (2007b) interpreted these starless condensations as being accumulated on the walls of the expanding shock front, but could not derive firm conclusions on their origin and nature.

This work aims at better understanding the nature of the dense cores in I20343, and its relation with the neighbouring more evolved objects. To achieve the goal we performed observations of molecular species obtained at high angular resolution with the Combined Array for Research in Millimeter Astronomy (CARMA) at 3 mm and the VLA at 1.3 cm. All selected molecular transitions are commonly used to characterize dense gas: (i)  $\text{NH}_3$  and  $\text{N}_2\text{H}^+$  are excellent tracers of dense and cold cores because either species do not suffer from depletion up to  $\sim 10^5 \text{ cm}^{-3}$ , and  $\text{NH}_3$  is extensively used as thermometer in both low- and high-mass star-forming regions; (ii)  $\text{NH}_2\text{D}$  provides an estimate of the degree of deuteration (with  $\text{NH}_3$ ). This combination of diagnostic lines was successfully used by Busquet et al. (2010) to identifying pre-protostellar cores in the proto-cluster associated with IRAS 20293+3952; (iii)  $\text{C}_2\text{H}$  and  $c\text{-C}_3\text{H}_2$  are both high-density photon dominated region (PDR) tracers useful to shed light on the interaction among the cold gas and the UV radiation field coming from IRS 1 and IRS 3.  $\text{C}_2\text{H}$  is also a tracer of cold gas (e.g. Beuther et al. 2008; Padovani et al. 2009). In this paper, we concentrate on the gas morphology, temperature and kinematics of the region adjacent to IRS 1 and IRS 3, and confirm the hypothesis proposed by Palau et al. (2007b) that IRS 3 is opening a cavity in the surrounding dense gas and starless material is being accumulated on the cavity walls. In Section 2 we describe the observations. The observational results are presented in Section 3, and discussed in Section 4. In Section 5 we summarize the main findings of the work and give a general conclusion.

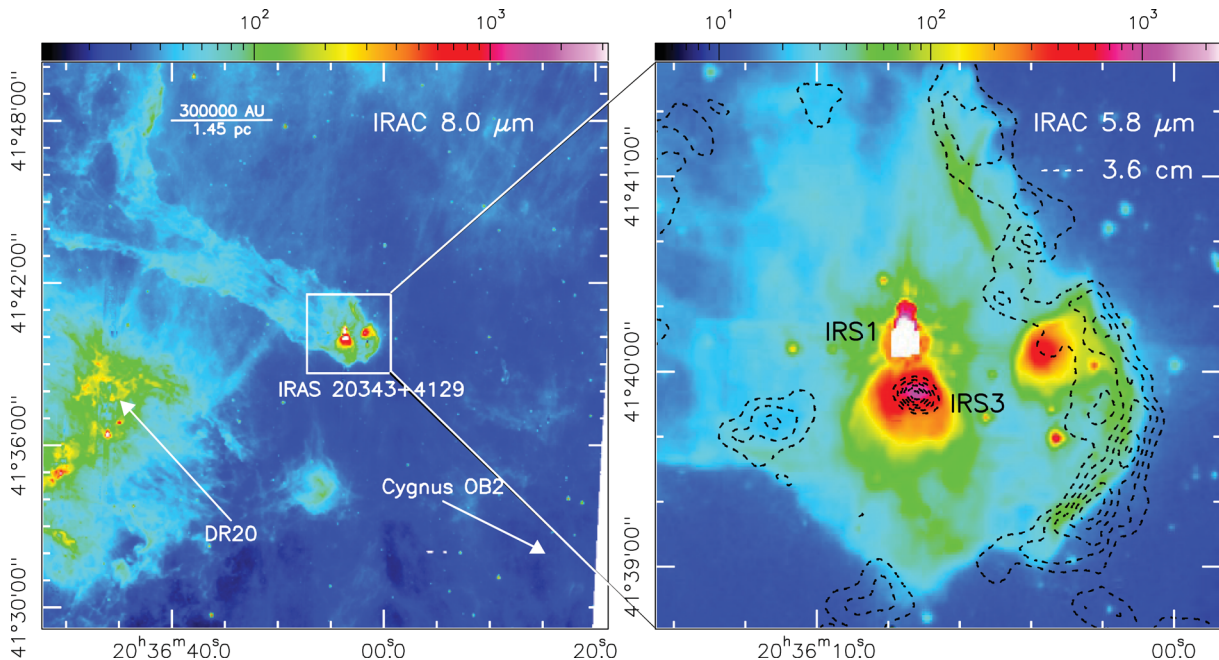


**Figure 1.** Large-scale view of the surroundings of IRAS 20343+4129 as seen by *Spitzer* at  $8.0 \mu\text{m}$ . The Cygnus OB2 association is located to the south-west as shown by the arrow. The enlargement panel to the right shows the region of our interest as it appears in the *Spitzer* image at  $5.8 \mu\text{m}$ , where we highlight the two infrared sources IRS 1 (saturated in the IRAC image) and IRS 3. In both panels, the colour scale units are  $\text{MJy sr}^{-1}$ . The dashed contours correspond to the 3.6 cm continuum emission detected by Carral et al. (1999) with the VLA (D-configuration).

**Table 1.** Observed tracers and basic parameters for the CARMA and VLA observations. The synthesized beam and  $1\sigma$  rms for CARMA observations are based on the combined configurations C+D (unless when differently specified).

Instrument/tracer <sup>a</sup>	Frequency <sup>b</sup> (GHz)	Synth. beam (arcsec <sup>2</sup> )	Linear resolution (pc)	$\Delta v$ (km s <sup>-1</sup> )	$1\sigma$ rms (Jy beam <sup>-1</sup> )	LAS <sup>c</sup> (arcsec)
<i>CARMA</i>						
3 mm continuum	86.4197	$4.80 \times 4.36$	$\sim 0.03$	–	0.0004	33
NH <sub>2</sub> D $J_{K_a, K_c} = 1_{1,1} - 1_{0,1}$ ( $F = 1 - 1$ )	85.9263	$3.32 \times 2.68$	$\sim 0.02$	0.07	0.045 <sup>d</sup>	33
C <sub>2</sub> H $N_{J, F} = 1_{3/2, 2} - 0_{1/2, 1}$	87.3169	$3.35 \times 2.72$	$\sim 0.02$	0.41	0.02	33
<i>ortho-c-C</i> <sub>3</sub> H <sub>2</sub> $J_{K_a, K_c} = 2_{1,2} - 1_{0,1}$ <sup>e</sup>	85.3389	$5.81 \times 4.54$	$\sim 0.034$	0.07	0.07	33
CCS $N_J = 7_6 - 6_5$	86.1814	$5.67 \times 4.84$	$\sim 0.035$	0.07	0.04	33
N <sub>2</sub> H <sup>+</sup> $J_{F_1} = 1_2 - 0_1$ ( $F = 3 - 2$ ) <sup>f</sup>	93.1737	$2.04 \times 1.94$	$\sim 0.013$	0.065	0.07	16
<i>VLA</i>						
7 mm continuum	43.3399	$4.67 \times 4.57$	$\sim 0.03$	–	0.0004	18
1.3 cm continuum	22.4601	$3.02 \times 2.98$	$\sim 0.02$	–	0.000057	34
NH <sub>3</sub> (1,1)	23.6945	$4.20 \times 3.19$	$\sim 0.025$	0.62	0.0035	34
NH <sub>3</sub> (2,2)	23.7226	$4.25 \times 3.19$	$\sim 0.025$	0.62	0.0035	34

<sup>a</sup> For the molecular transitions, in the text we will use the following abbreviations: NH<sub>2</sub>D (1<sub>1,1</sub> – 1<sub>0,1</sub>) = NH<sub>2</sub>D (1–1); C<sub>2</sub>H (1<sub>3/2,2</sub> – 0<sub>1/2,1</sub>) = C<sub>2</sub>H (1–0); *c*-C<sub>3</sub>H<sub>2</sub> (2<sub>1,2</sub> – 1<sub>0,1</sub>) = *c*-C<sub>3</sub>H<sub>2</sub> (2–1); N<sub>2</sub>H<sup>+</sup> (1<sub>2</sub> – 0<sub>1</sub>) = N<sub>2</sub>H<sup>+</sup> (1–0).

<sup>b</sup> Rest frequency of the transition listed in Column 1.

<sup>c</sup> Largest angular scale (at half power) detectable by the interferometer, estimated from the minimum baseline of the array configuration, and following the appendix in Palau et al. (2010). For the lines observed in C- and D-configuration, this refers to the merged uv coverage.

<sup>d</sup> Sensitivity in the merged C+D channel maps smoothed to a spectral resolution of 0.1 km s<sup>-1</sup>.

<sup>e</sup> Observed in D-configuration only.

<sup>f</sup> Observed in C-configuration only.

## 2 OBSERVATIONS AND DATA REDUCTION

### 2.1 CARMA

3 mm CARMA observations of I20343 were obtained on 2010 Mar 29 in C- and on 2010 May 01 in D-configuration under good weather conditions for observations at 3 mm, characterized by about 5 mm of precipitable water and atmospheric noise rms of about 300  $\mu$ m as measured on a baseline of 100 m at the frequency of 225 GHz. The phase centre was the same as in Palau et al. (2007b), namely: RA (J2000) = 20<sup>h</sup>36<sup>m</sup>07<sup>s</sup>.3 and Dec. (J2000) = 41<sup>o</sup>39'57".2. The local standard of rest velocity of the cloud is assumed to be 11.5 km s<sup>-1</sup>, as determined from single-dish ammonia observations (Sridharan et al. 2002). The primary beam of the 10 m and 6 m dishes at about 85 GHz is  $\sim 73$  and 121 arcsec, respectively. The single-sideband system temperature during the observations was below 150 K. During C-configuration observations, the correlator provided four bands, which were configured to observe the continuum, the C<sub>2</sub>H, the NH<sub>2</sub>D and the N<sub>2</sub>H<sup>+</sup> lines simultaneously. D-array observations were obtained with the new CARMA correlator, which provides more bands. Two 500 MHz bands were used to observe the continuum and five bands set up to observe the C<sub>2</sub>H, N<sub>2</sub>H<sup>+</sup>, NH<sub>2</sub>D, CCS and *c*-C<sub>3</sub>H<sub>2</sub> line emission. The pass-band was calibrated by observing 1733–130; flux calibration was set by observing MWC349. The estimated uncertainty of the absolute flux calibration is 10 per cent, and it is determined from periodic observations of MWC349. Atmospheric and instrumental effects were corrected by observing the nearby quasar 2007+404 every 15 min.

The tracers observed and the main observational parameters (frequency, synthesized beam, linear resolution, spectral resolution,  $1\sigma$  rms channel noise, largest detectable angular scale) are reported in Table 1. The CCS line is the only undetected transition and will be not discussed in the following. The continuum was derived by averaging the 500 MHz bands. Visibility data were edited

and calibrated with the MIRIAD package. A minor flagging of the data was performed using the UVFLAG task, mainly to remove the intervals characterized by the bad atmospheric phase coherence. The channel spacing and the corresponding  $1\sigma$  rms noise are shown in Table 1. Merging the visibilities obtained in C- and D-configuration, imaging, deconvolution and analysis of channel maps and continuum were performed using the standard tasks of the GILDAS<sup>1</sup> package (e.g. UVMERGE, UVMAP, CLEAN). Images were created applying natural weighting to the visibilities.

### 2.2 VLA

I20343 was observed with the VLA<sup>2</sup> at 1.3 and 0.7 cm on 2007 Mar 26 using the array in the D-configuration.<sup>3</sup> The phase centre of the observations was RA (J2000) = 20<sup>h</sup>36<sup>m</sup>07<sup>s</sup>.51; Dec. (J2000) = 41<sup>o</sup>40'00".9. The data reduction followed the VLA standard guidelines for calibration of high-frequency data, using the NRAO package AIPS. The absolute flux scale was set by observing the quasar 1331+305 (3C286), for which we adopted a flux of 2.52 Jy at 1.3 cm, and 1.45 Jy at 0.7 cm. The quasar 2015+371, with a bootstrapped flux of  $1.39 \pm 0.02$  Jy at 1.3 cm and  $2.1 \pm 0.2$  Jy at 0.7 cm, was observed regularly to calibrate the gains and phases. Final images were produced with the robust parameter of Briggs (1995) set to 5, corresponding to natural weighting. At 7 mm we

<sup>1</sup> The GILDAS software is developed at the IRAM and the Observatoire de Grenoble, and is available at <http://www.iram.fr/IRAMFR/GILDAS>

<sup>2</sup> The VLA is operated by the National Radio Astronomy Observatory (NRAO), a facility of the National Science Foundation operated under cooperative agreement by Associated Universities, Inc.

<sup>3</sup> The VLA continuum observations presented in this work correspond to project AP525. Another project, AP533, was undergone at 3.6, 2 and 0.7 cm, but due to technical problems the data of AP533 project were lost.

applied a taper at 60 k $\lambda$  with the aim of recovering faint extended emission, but no emission was detected at this wavelength.

The VLA was also used to map the  $(J, K) = (1, 1)$  and  $(2, 2)$  inversion transitions of the ammonia molecule on 2001 July 23, with the array in the C-configuration. The phase centre was set to RA(J2000) = 20<sup>h</sup>36<sup>m</sup>08<sup>s</sup>.013; Dec.(J2000) = +41<sup>°</sup>39'56".93. The full width at half-maximum (FWHM) of the primary beam at the observed frequency was  $\sim 110$  arcsec, and the range of projected baselines was 2.59 to 267.20 k $\lambda$ . The absolute flux calibration was performed by using 3C286, adopting a flux density at 1.3 cm of 2.41 Jy. The phase calibrator was QSO 2013+370, with a 1.3 cm bootstrapped flux density of  $2.34 \pm 0.04$  Jy, and 3C273 was used as the bandpass calibrator. The NH<sub>3</sub>(1,1) and NH<sub>3</sub>(2,2) lines were observed simultaneously in the four IF correlator mode of the VLA (with two polarizations for each line), providing 63 channels with a spectral resolution of 0.62 km s<sup>-1</sup> across a bandwidth of 3.13 MHz, plus an additional continuum channel containing the central 75 per cent of the total bandwidth. The bandwidth was centred at the systemic velocity  $V_{\text{LSR}} = 11.5$  km s<sup>-1</sup> (Sridharan et al. 2002) for the NH<sub>3</sub>(1,1) line, and at  $V_{\text{LSR}} = 6.5$  km s<sup>-1</sup> for the NH<sub>3</sub>(2,2) line (to cover the main and one of the satellite components). Data were calibrated using standard procedures of AIPS, and imaging was performed by applying a taper in the  $uv$ -data of 50 k $\lambda$  and using natural weighting to recover the faint and extended emission. The synthesized beams and rms noises for all the VLA observations are listed in Table 1.

### 3 RESULTS

#### 3.1 Continuum emission maps

In Fig. 2 the 3 mm (CARMA, C+D configuration, solid contours) and 1.3 cm (VLA, D-configuration, dashed contours) continuum emission maps are shown. As reference, we overplot the 1.3 mm continuum emission observed by Palau et al. (2007b, obtained with about a factor of 1.5 better angular resolution) as well as the direction of the lobes of the <sup>12</sup>CO outflow originated by IRS 1 and the (rough) edge of the fan-shaped H<sub>2</sub> emission associated with IRS 3 (Kumar et al. 2002).

The 3 mm continuum emission is resolved into five main condensations, which we call MMA, MMB, MMC, MMD and MME in order of increasing RA. The brightest are MME and MMA, east and west of IRS 3, respectively. From Fig. 2 we note that MME roughly coincides with a 1.3 mm continuum peak (Palau et al. 2007b), while the westernmost one, MMA, encompasses three peaks seen at 1.3 mm with Submillimete Array (SMA). The faintest core, MMC, is detected towards IRS 1. Two more 3 mm condensations, MMD and MMB, are not detected at 1.3 mm. Specifically, MMB is clearly detected close to IRS3, with a shift of only 4 arcsec to the northeast.

The most evident differences among the 3 and 1.3 mm continuum maps are that at 3 mm core MME (MM7 in Palau et al. 2007b) is more extended, and the eastern and western cores are connected by a filamentary emission passing through IRS 3 which is undetected at 1.3 mm. Both differences are probably just the consequence of CARMA being sensitive to larger structures than the SMA. We estimated that the SMA in the observations of Palau et al. (2007b) was sensitive to structures with FWHM <9 arcsec (using the minimum baseline of the observations and following Palau et al. 2010), while CARMA using C+D configurations was sensitive to structures <33 arcsec (Table 1), allowing CARMA to recover more extended emission.

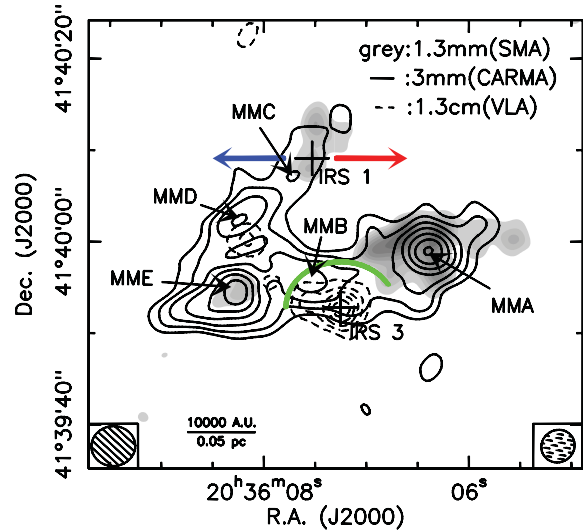


**Figure 2.** Continuum emission obtained with CARMA at 3 mm (solid contours) and with the VLA at 1.3 cm (dashed contours) towards I20343. The solid contours start from the  $3\sigma$  rms level ( $1.2 \times 10^{-3}$  Jy beam<sup>-1</sup>) and are in steps of  $1\sigma$  rms. The dashed first contour and step correspond to the  $3\sigma$  rms level ( $1.5 \times 10^{-5}$  Jy beam<sup>-1</sup>) and are in steps of  $1\sigma$  rms. The grey-scale indicates the 1.3 mm continuum emission observed by Palau et al. (2007b) with the SMA (levels = 10 per cent of the maximum, first level = 20 per cent of the maximum). The crosses indicate the two infrared sources identified by Kumar et al. (2002). Red and blue arrows highlight the direction of the blue- and redshifted emission detected in <sup>12</sup>CO (2–1) by Palau et al. (2007b). The green arc roughly shows the fan-shaped feature detected in H<sub>2</sub>  $\mu$ m associated with IRS 3 (Kumar et al. 2002), interpreted as an expanding cavity by Palau et al. (2007b). The ellipse at bottom-left corresponds to the CARMA synthesized beam ( $4.8 \times 4.4$  arcsec<sup>2</sup>, at PA 92°). The dashed ellipse at bottom-right is the VLA synthesized beam ( $3.71 \times 3.50$  arcsec<sup>2</sup>, at PA -56.2°).

As shown in Fig. 2, the continuum emission at 1.3 cm is dominated by one strong and compact source with its emission peak (20<sup>h</sup>36<sup>m</sup>07.3<sup>s</sup>, +41<sup>°</sup>39'52") coincident with IRS 3, and matching well the fan-shaped H<sub>2</sub> emission detected by Kumar et al. (2002). A Gaussian fit to this compact centimetre source yields a peak intensity of 0.8 mJy beam<sup>-1</sup>, a flux density of 1.3 mJy and a deconvolved size of  $4.3 \times 1.0$  arcsec<sup>2</sup>, with PA = 78°, corresponding to a size of 6000 au in the east–west direction (and an unresolved size in the north–south direction). In addition to the compact 1.3 cm source associated with IRS 3, there is a secondary peak at around 6 $\sigma$  which falls 2 arcsec to the south of MMD, and faint emission joining this secondary peak and the centimetre source in IRS 3, suggesting that the two peaks of centimetre emission could be linked.

#### 3.2 Distribution of the Integrated intensity of molecular line emission

##### 3.2.1 Molecular tracers observed with CARMA

The maps of the integrated intensity of the lines observed and detected with CARMA (see Table 1) are shown in Fig. 3. The emission map of each tracer has been superimposed on the images obtained from the *Spitzer Space Telescope* in the four mid-IR IRAC bands (centred at 3.6, 4.5, 5.8 and 8  $\mu$ m, respectively). The location of the near-infrared sources IRS 1 and IRS 3 is also indicated, along with the direction of the outflow centred on IRS 1 and the edge of the H<sub>2</sub> emission associated with IRS 3, as in Fig. 2. We also superimpose

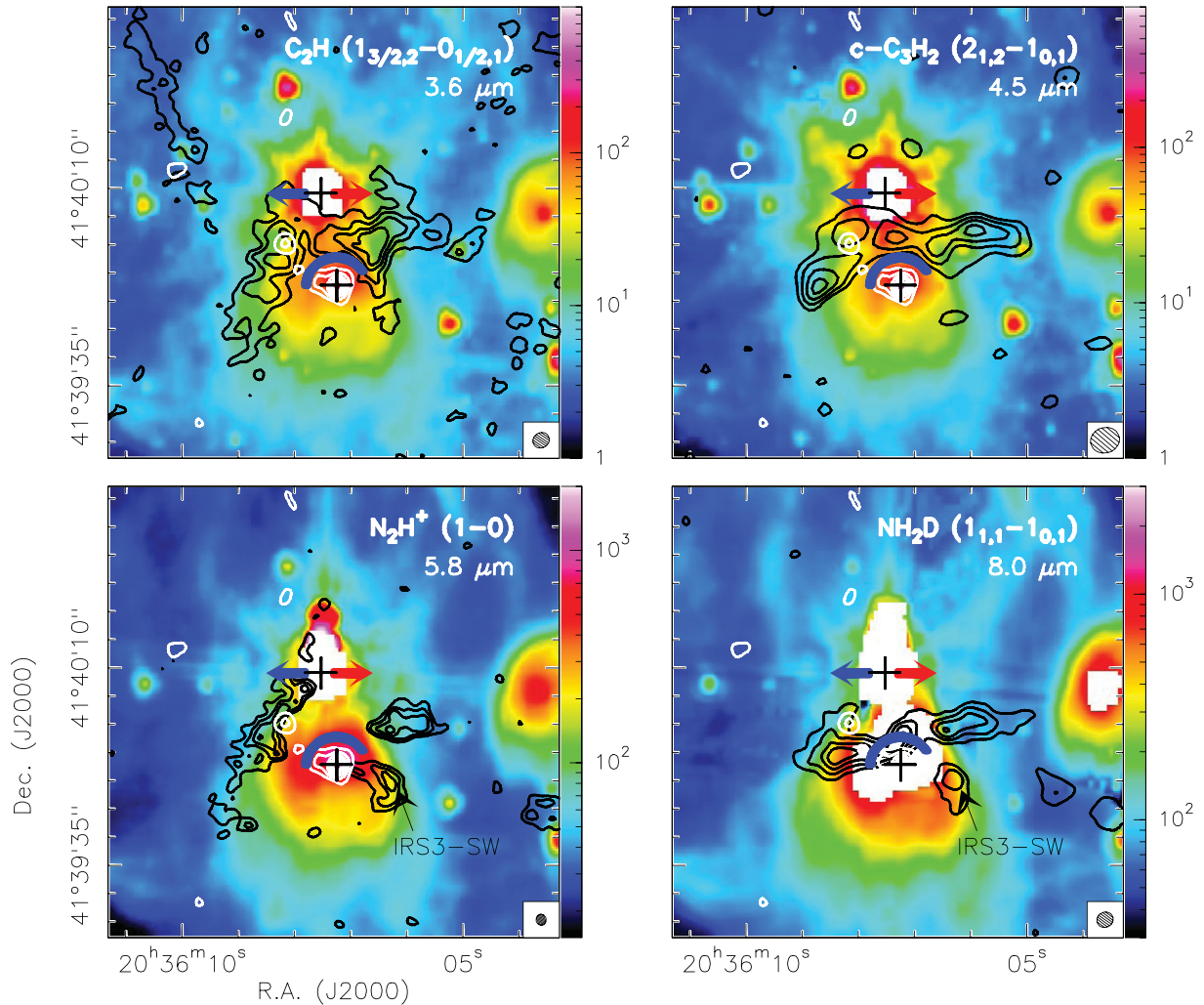


**Figure 3.** Integrated maps of the molecular lines detected with CARMA (Table 1) towards I20343 and superimposed on the images obtained in the *Spitzer*-IRAC bands (3.6  $\mu\text{m}$ , 4.5  $\mu\text{m}$ , 5.8  $\mu\text{m}$ , 8  $\mu\text{m}$ , colour scale in  $\text{MJy sr}^{-1}$  units). In each panel, black contours depict the velocity-averaged emission of the transition labelled at the top-right corner (the corresponding synthesized beam is shown in the bottom-right corner). For all lines, the emission has been averaged over all the velocity channels with signal, except for  $\text{N}_2\text{H}^+$  (bottom-left panel) for which the integrated emission was averaged over the main group of hyperfine components only. For  $\text{C}_2\text{H}$  and  $\text{NH}_2\text{D}$ , first contour and step correspond to the 20 per cent level of the maximum (corresponding roughly to the  $3\sigma$  rms level of the averaged map), while for  $c\text{-C}_3\text{H}_2$  and  $\text{N}_2\text{H}^+$  contours start from the 30 per cent level of the maximum and are in steps of 20 per cent. The white contours represent the VLA 1.3 cm (*K* band) continuum image (same contours as in Fig. 2). The position of IRS 1 and IRS 3, the associated outflow and fan-shaped  $\text{H}_2$  emission are shown as in Fig. 2.

the 1.3 cm continuum emission detected in this work (see Fig. 2), which marks clearly the  $\text{H II}$  region associated with IRS 3.

The molecular gas seems to be squeezed in between the two dominant mid-IR sources IRS 1 and IRS 3 in all molecules except  $\text{N}_2\text{H}^+$ . Other compact mid-IR sources are present in the region but do not seem to be associated with any clear molecular counterpart. The diffuse IR nebulosity, especially evident in the 5.8 and 8  $\mu\text{m}$  bands, is probably emission from small dust grains distributed around I20343 becoming brighter at longer wavelengths. Some of the diffuse emission detected at 8  $\mu\text{m}$  may also be polycyclic aromatic hydrocarbons (PAHs) emission (e.g. Peeters et al. 2002).

The morphology of the integrated intensity of  $c\text{-C}_3\text{H}_2$  (2-1) and  $\text{C}_2\text{H}$  (1-0) delineates clearly a cavity around IRS 3 (top panels of Fig. 3), providing a strong support to the hypothesis proposed by Palau et al. (2007b), namely that IRS3 is most likely a more evolved intermediate-mass star creating a cavity. The  $\text{C}_2\text{H}$  emission is more extended than that of  $c\text{-C}_3\text{H}_2$ , perhaps due to the smaller sensitivity

that we have in the  $c\text{-C}_3\text{H}_2$  channel maps (see Table 1). Specifically, a narrow filament extended  $\sim 30$  arcsec is clearly detected north-east of the field centre (Fig. 3, top-left panel), inclined roughly as the tail of the mid-IR cometary shape (see Fig. 1), suggesting that the two features can have the same origin.

The bottom panels in Fig. 3 show the integrated emission of the two nitrogen-bearing species  $\text{N}_2\text{H}^+$  and  $\text{NH}_2\text{D}$ . The emission in  $\text{N}_2\text{H}^+$  consists mainly of one cloud to the east of IRS 3 elongated in the southeast–north-west direction, and extending up to IRS 1, and two smaller clouds, one immediately to the south-west of IRS 3 with no continuum counterpart (called IRS3-SW), and the other associated with MMA. In addition, there is one clump about 1 arcmin to the west of IRS 3, almost at the border of the bright rim, which falls on a region with no infrared emission associated. On the other hand, the emission of  $\text{NH}_2\text{D}$  consists mainly of one filament elongated in the east–west direction, passing through IRS 3, and with some emission at IRS3-SW. The  $\text{N}_2\text{H}^+$  clump 1 arcmin to the west

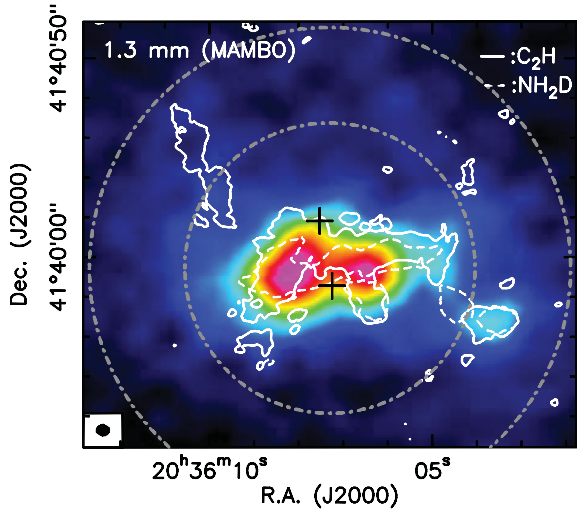


**Figure 4.** Integrated emission of molecular tracers (white contours) superimposed on the image of I20343 in MAMBO at 1.2 mm (Beuther et al. 2002). The solid white contour depicts the 15 per cent level of the zero-order moment map of  $C_2H$  (1–0). The dashed white contour corresponds to the 15 per cent level of the zero-order moment map for the  $NH_2D$  (1–1) line. The ellipse in the bottom-left corner shows the CARMA synthesized beam for the  $C_2H$  map and it is almost coincident to that of the  $NH_2D$  map. The grey dot-dashed circles represent the primary beams of the CARMA 10 and 6 m dishes (73 and 121 arcsec), respectively.

of IRS 3 is detected also in  $NH_2D$ , but looks more extended in  $NH_2D$ . However, this can be just an effect of the different angular resolution and different filtering of extended emission, as  $NH_2D$  was observed with C+D configuration while  $N_2H^+$  was observed in C-configuration only (see Table 1).

If we put together the two mostly extended molecular tracers, namely  $C_2H$  and  $NH_2D$ , we can notice a sort of ‘snake-like’ filament of molecular gas (Fig. 4) extending from the south-western side of I20343, clearly detected in  $NH_2D$ , up to the north-eastern corner, in which a long and narrow filament is detected in  $C_2H$ . The bulk of the emission is in between IRS 1 and IRS 3. This ‘snake-like’ filament matches very well the 1.2 mm continuum emission detected with MAMBO (Beuther et al. 2002, Fig. 4), and its SW–NE inclination follows roughly the ‘head–tail’ orientation of the mid-IR diffuse cometary emission (Fig. 1), suggesting a possible common origin. However, the highest sensitivity region of the CARMA maps, i.e. the field of view of the 10 m dishes ( $\sim 73$  arcsec), includes only the central region of the filament (see Fig. 4). For this reason, in this work we focus on the centre of I20343, where the interaction between the two brightest IR sources and the surrounding molecular gas seems predominant, and plan a large interferometric mosaic that will allow us to unveil the overall distribution of the molecular gas and its relation with all the IR sources.

### 3.2.2 Ammonia (1,1) and (2,2) inversion transitions

The integrated intensity maps of  $NH_3$  (1,1) and (2,2) are presented in Fig. 5. In the (1,1) line, the emission resembles that seen with CARMA in the 3 mm continuum. Four main peaks are detected, which roughly correspond to those detected in the 3 mm continuum. On the other hand, none of the 1.3 mm continuum peaks identified by Palau et al. (2007b) exactly coincides with any of the  $NH_3$  (1,1) peaks, despite the similar angular resolution. The  $NH_3$  (1,1)

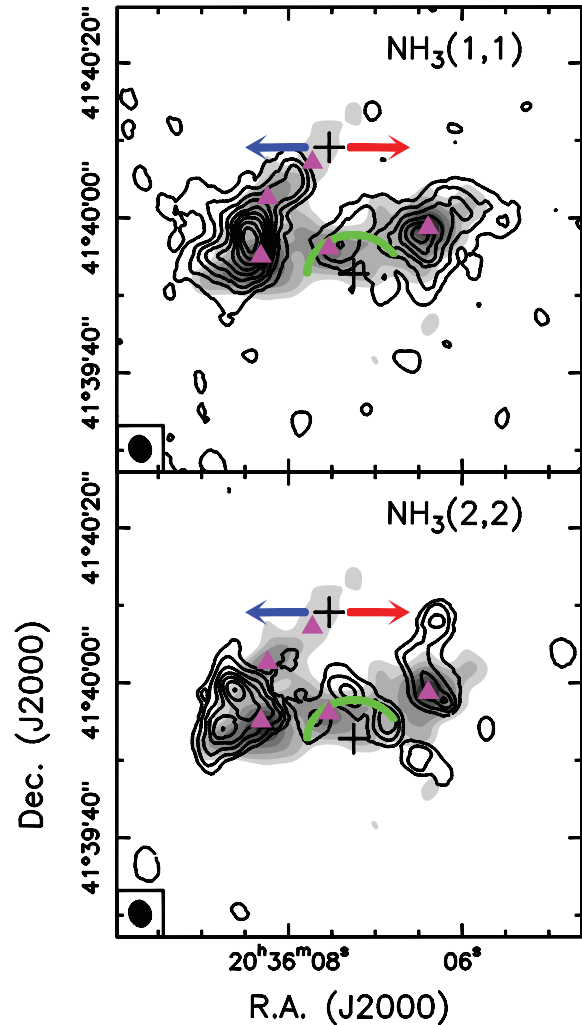


**Figure 5.** Top panel: integrated emission map of the ammonia (1,1) inversion transition (contours) observed with the VLA towards I20343, superimposed on the 3 mm continuum (CARMA, grey-scale). First contour level and step are the 10 per cent of the peak ( $224 \text{ Jy beam}^{-1} \text{ m s}^{-1}$ ). The ellipse at bottom left represents the VLA synthesized beam ( $4.20 \times 3.19 \text{ arcsec}^2$ , at PA  $\sim 11^\circ$ ). Purple triangles pinpoint the 3 mm continuum peaks (see Fig. 2). All other symbols (crosses, arrows and semi-ellipse) represent the same as in Fig. 2. Bottom panel: same as top panel for the (2,2) inversion transition. First contour level and step are the 15 per cent of the peak ( $57 \text{ Jy beam}^{-1} \text{ m s}^{-1}$ ). The synthesized beam in this case is  $4''.25 \times 3''.19$ , at P.A.  $\sim 13^\circ$ .

emission reveals two main clouds, one to the east and the other to the west of IRS 3. The eastern cloud includes MMD and MME and appears elongated in the southeast–north–west direction, similar to the  $N_2H^+$  eastern cloud and to the 3 mm continuum emission. The western cloud has a condensation near MMB (near IRS 3) and another condensation near MMA. The overall emission in the western cloud is elongated in the east–west direction. We stress that  $NH_3$  (1,1) emission is marginally detected also towards IRS 3 and the cavity driven by it, as for the 3 mm continuum. On the other hand, the millimetre continuum sources associated with IRS 1 as well as the  $^{12}CO$  outflow lobes are not detected in ammonia. The  $NH_3$  (2,2) transition is clearly detected towards the eastern side of MME, where two peaks are resolved. The  $NH_3$  (2,2) line emission around IRS 3 and towards the west is clumpy, peaking towards MMA and near MMB and IRS3-SW.

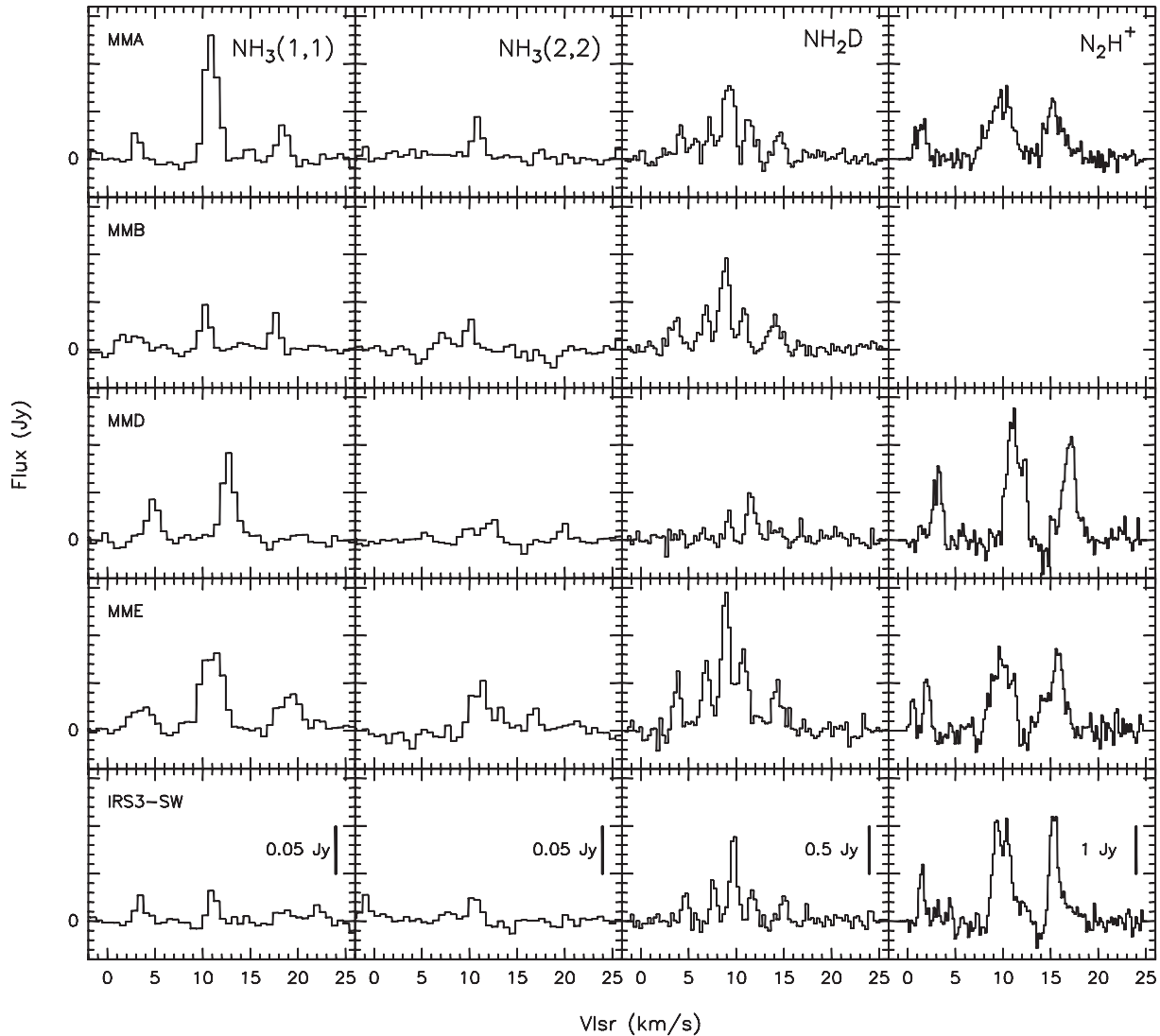


**Figure 6.** Spectra of the detected transitions of  $\text{NH}_3$ ,  $\text{NH}_2\text{D}$  and  $\text{N}_2\text{H}^+$  at the position of the 3 mm continuum condensations (except MMC, undetected in all the lines) and the molecular condensation IRS3-SW. The polygon used to extract the spectra corresponds to: the  $5\sigma$  rms contour of the 3 mm continuum image for MMA and MME; the  $3\sigma$  rms contour of the 3 mm continuum image for MMB and MMD; the  $5\sigma$  rms contour of the integrated emission of  $\text{NH}_2\text{D}$  (1–1) for IRS3-SW.

From a comparison of the N-bearing to the C-bearing species, both  $\text{C}_2\text{H}$  and  $c\text{-C}_3\text{H}_2$  highlight clearly the cavity associated with IRS 3 (see top panels in Fig. 3), while  $\text{NH}_2\text{D}$  and  $\text{NH}_3$  trace emission extending east–west passing through IRS 3 (see Fig. 5 and bottom panels of Fig. 3) more similar to that seen in the 3 mm continuum map. Thus, there seems to be a chemical dichotomy in I20343 among carbon- and nitrogen-bearing molecules. The exception is represented by  $\text{N}_2\text{H}^+$ , detected away from IRS 3. This molecule appears to trace the part of the cloud less disrupted by the expanding cavity.

The spectra of the  $\text{NH}_3$ (1,1) and  $\text{NH}_3$ (2,2) emission, integrated within the  $5\sigma$  contour polygon of the 3 mm continuum image (except for MMB and MMD, where we used the  $3\sigma$  contour), are shown in Fig. 6. For IRS3-SW, we used the  $5\sigma$  rms contour of the  $\text{NH}_2\text{D}$  (1–1) line-integrated emission (Fig. 3, bottom-right panel). To compare the different molecular species, in Fig. 6 we also show the integrated spectra of  $\text{NH}_2\text{D}$  and  $\text{N}_2\text{H}^+$  extracted using the same polygons. We do not show the spectra towards MMC because this

core is undetected in  $\text{NH}_2\text{D}$  and  $\text{NH}_3$  (2,2), and marginally detected in the other lines. Among all the  $\text{NH}_3$  (1,1) spectra, MMA shows the strongest emission, and MME shows the broadest lines, of up to  $2.2 \text{ km s}^{-1}$ . Such a large line broadening in MME could be due to a double velocity component, as suggested by the  $\text{N}_2\text{H}^+$  spectrum which has 10 times better spectral resolution. Concerning MMB, MMD and IRS3-SW  $\text{NH}_3$  (1,1) spectra, it is striking to see the anomaly in the inner satellite hyperfine lines, with one inner satellite clearly detected above  $5\sigma$  and the other inner satellite being undetected. The anomaly for the non-local thermodynamic equilibrium (LTE) case due to hyperfine selective photon trapping affects only the outer satellites (red stronger than blue; Stutzki & Winnewisser 1985), allowing us to rule out this possibility in I20343. Rather, anomalies of one inner satellite being stronger than the other have been observed in several works (Lee et al. 2002; Longmore et al. 2007; Purcell et al. 2009) and explained as being due to systematic motions, following the theoretical work of Park (2001). Park (2001) shows that if the core is contracting, the inner

**Table 2.**  $\text{NH}_3$ ,  $\text{N}_2\text{H}^+$  and  $\text{NH}_2\text{D}$  line parameters for the 3 mm continuum cores (except MMC) and the molecular core IRS3-SW. The parameters have been derived from the spectra shown in Fig. 6 using the fitting procedure described in Section 3.2.2.

Core	$\text{NH}_3$			$T_{\text{rot}}$ (K)	$\text{N}_2\text{H}^+$			$\text{NH}_2\text{D}$		
	$T_{\text{ex}}$ (K)	$\Delta v$ ( $\text{km s}^{-1}$ )	$\tau^a$		$T_{\text{ex}}$ (K)	$\Delta v$ ( $\text{km s}^{-1}$ )	$\tau^a$	$T_{\text{ex}}$ (K)	$\Delta v$ $\text{km s}^{-1}$	$\tau^a$
MMA	– <sup>b</sup>	1.52	>1	18 (1)	7	1.63	4.6	17	1.05	2.8
MMB	9.7	1.03	3.5	20 (7)	–	–	–	20	1.03	2.5
MMD	21.5	1.21	1.4	13 (2)	14	0.9	5.2	41	0.89	0.38
MME	19.8	2.2	1.5	18 (3)	6	0.7	10	26	1.01	3.2
IRS3-SW	7.9	1.03	3.2	23 (7)	13	0.7	3.3	23	0.72	1.8

<sup>a</sup>Total opacity of the line.

<sup>b</sup>In this core the excitation temperature for the main and the satellite lines of the  $\text{NH}_3$  (1,1) transition is probably different. See Appendix A for the detailed discussion on the derivation of the physical parameters from  $\text{NH}_3$ .

blue satellite should be stronger than the inner red satellite for a systematic motion in the range of 0.4–1  $\text{km s}^{-1}$ , and for a range of  $\text{H}_2$  number densities and  $\text{NH}_3$  column densities, which are consistent with those derived by us (as we will show in Section 3.4). This is the case of MMD and IRS3-SW. On the other hand, if the core is undergoing expanding motions, the prediction is that the inner red satellite should be stronger than the inner blue satellite, as seen for the case of MMB. Thus, it seems that for these three clumps the  $\text{NH}_3$ (1,1) anomalous intensity of the hyperfine components is consistent with contracting/expanding motions.

The MMA  $\text{NH}_3$ (1,1) spectrum is a very special case, as the inner satellites are detected at an intensity smaller than that expected for LTE conditions (maximum main-to-satellite ratio in LTE is 3.6, while the ratio for MMA is 4.3). This could be explained if the opacity is high and the excitation temperature for the main line and the satellites is different, with the satellites having a lower excitation temperature (and hence a smaller main beam temperature). A detailed discussion on the temperature ratio between main line and satellites leads to a possible non-isothermal core made of two layers, with the external one being hotter than the inner one. If this interpretation is correct, core MMA could be heated externally, perhaps by IRS 3 and/or the infrared sources west of I20343 (see right-hand panels in Figs 1 and 3). We give details of this explanation in Appendix A.

We fitted the  $\text{NH}_3$ ,  $\text{NH}_2\text{D}$  and  $\text{N}_2\text{H}^+$  spectra in order to derive the physical parameters of the gas traced by these molecules. To take into account the line hyperfine structure, we followed the method described in the CLASS user manual.<sup>4</sup> The  $\text{NH}_3$  (1,1),  $\text{NH}_2\text{D}$  (1–1) and  $\text{N}_2\text{H}^+$  (1–0) lines were fitted this way, while we fitted the  $\text{NH}_3$  (2,2) lines with Gaussians. The derived fit parameters are reported in Table 2, except the line velocities that will be extensively discussed in Section 3.3. These parameters have been used to derive the molecular column densities, the derivation of which will be described in Section 4.2. To fit the hyperfine structure of MMB, MMD and IRS3-SW, we used only the detected satellite and the main line, in order to obtain reliable opacities. For  $\text{NH}_3$ , in Table 2 we list also the rotation temperature,  $T_{\text{rot}}$ , obtained from the (2,2)-to-(1,1) intensity ratio following the method outlined in Busquet

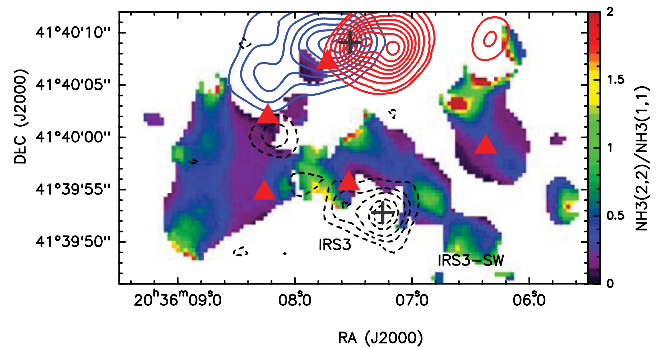


**Figure 7.** Colour scale: ratio of the integrated  $\text{NH}_3$  emission (2,2)/(1,1). Red triangles indicate the 3 mm continuum peaks, which correspond to (from east to west) MME, MMD, MMC, MMB and MMA. The black-dashed contours indicate the VLA 1.3 cm emission (2.5, 5, 7.5, 12, 15 times  $50 \mu\text{Jy beam}^{-1}$ ). The blue/red solid contours depict the high-velocity CO (2–1) blueshifted/redshifted emission (Palau et al. 2007b). Blue contours range from 10 to 99 per cent in steps of 12 per cent of the peak intensity ( $21.335 \text{ Jy beam}^{-1} \text{ km s}^{-1}$ ); red contours are 6, 12 to 99 per cent in steps of 12 per cent of the peak intensity ( $41.781 \text{ Jy beam}^{-1} \text{ km s}^{-1}$ ).

et al. (2009), which is based on the discussion presented in Ho & Townes (1983). These range from 13 K (in MMD) to 23 K (in IRS3-SW).

In order to obtain a first approach to temperature variations of the dense gas across I20343, we computed the ratio of the integrated  $\text{NH}_3$  (2,2)/(1,1), which has been shown to be a reasonable approach to the kinetic temperature (e.g. Torrelles et al. 1993; Zhang et al. 2002). The result is shown in Fig. 7. As can be seen from the figure, the ratio is largest towards three main regions: near IRS 3 (MMB and IRS3-SW), to the north of MMA and to the eastern side of MME. Thus, the spectra towards MMA, which can be explained with external heating, is consistent with the 22/11 ratio map, which reveals that the heating comes most likely from the north of MMA. Interestingly, the north of MMA is spatially coinciding with the redshifted CO outflow lobe driven by IRS 1, suggesting that the outflow and the dense gas are interacting (Fig. 7). Most intriguing is the high ratio seen at the eastern side of MME, which extends all along the north–south direction and is seen westwards of the  $\text{H}_2$  extended emission reported by Kumar et al. (2002). Such a spatial coincidence is suggestive of a possible relation between the high 22/11 ratio and the  $\text{H}_2$  emission. Finally, the high 22/11 ratio near

<sup>4</sup>The CLASS program is part of the GILDAS software, developed at the IRAM and the Observatoire de Grenoble, and is available at <http://www.iram.fr/IRAMFR/GILDAS>

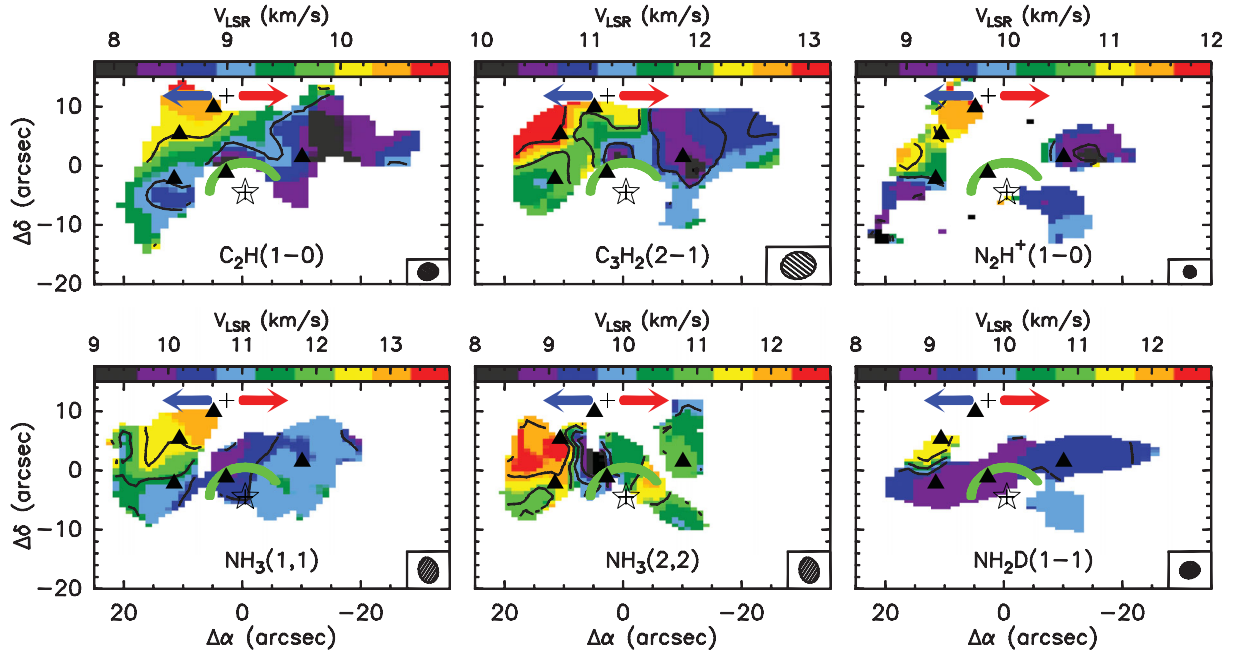


**Figure 8.** Maps of the line peak velocity for all detected molecular lines. Top panels show (from left to right):  $C_2H(1-0)$ ,  $c-C_3H_2(2-1)$  and  $N_2H^+(1-0)$ . Contours are in steps of  $1 \text{ km s}^{-1}$ , and range from  $8$  to  $11 \text{ km s}^{-1}$  for  $C_2H$ ,  $10.5$  to  $13.5$  for  $c-C_3H_2$ ,  $9$  to  $12 \text{ km s}^{-1}$  for  $N_2H^+$ . Bottom panels show (from left to right)  $NH_3(1,1)$ ,  $NH_3(2,2)$  and  $NH_2D(1-1)$ . Contours are in steps of  $1 \text{ km s}^{-1}$ , and range from  $9.5$  to  $13.5 \text{ km s}^{-1}$  for  $NH_3(1,1)$ ,  $9$  to  $13 \text{ km s}^{-1}$  for  $NH_3(2,2)$ ,  $8.5$  to  $12.5 \text{ km s}^{-1}$  for  $NH_2D$ . In each panel, the ellipse in the bottom-right corner represents the CARMA or VLA synthesized beam. The black triangles pinpoint the  $3 \text{ mm}$  continuum peaks (Section 3.1). The position of IRS 1 and IRS 3, as well as the associated outflow and fan-shaped  $H_2$  emission, is depicted in each panel as in Fig. 2.

IRS 3 could be indicative of direct heating by the UC H II region associated with IRS 3.

### 3.3 Kinematics

To inspect the velocity field, we have extracted from the interferometric channel maps spectra of the molecular transitions detected on grids with regular spacings ( $1.5 \times 1.5 \text{ arcsec}^2$  for  $C_2H$ ,  $2.5 \times 2.5 \text{ arcsec}^2$  for  $c-C_3H_2$ ,  $1 \times 1 \text{ arcsec}^2$  for  $N_2H^+$ ,  $1.6 \times 1.5 \text{ arcsec}^2$  for  $NH_2D$  and  $NH_3$ ). The spectra extracted have been fitted following different methods: for  $C_2H(1-0)$ ,  $c-C_3H_2(2-1)$  and  $NH_3(2,2)$  we assumed Gaussian lines, while for  $N_2H^+(1-0)$ ,  $NH_2D(1-1)$  and  $NH_3(1,1)$  we fitted the lines following the method described in Section 3.2.2 to take into account their hyperfine structure.

#### 3.3.1 Line peak velocities

Fig. 8 shows maps obtained from the line peak velocities. In all tracers the radial velocities are predominantly blueshifted to the west and redshifted to the north-east. The east–west velocity gradient is not uniform and suggests a possible torsion of the gas. Interestingly, the inclination of this gradient with respect to the line of sight is opposite to that of the outflow associated with IRS 1, since the blue lobe of the outflow is located on the side where the dense gas is redshifted, and vice versa. In general, all tracers with emission near IRS 3 (in MMB) show that the gas is blueshifted at this position.

#### 3.3.2 Line widths

Maps of the line widths are presented in Fig. 9. The measured line broadenings are generally a factor of  $>3$  higher than the thermal broadening, expected to be of the order of  $\sim 0.1\text{--}0.3 \text{ km s}^{-1}$ ,

indicating that the gas kinematics is largely dominated by non-thermal motions. This finding confirms previous studies in similar intermediate- to high-mass protoclusters (e.g. Palau et al. 2007a; Fontani et al. 2009; Busquet et al. 2010), and represents one of the most important differences between these dense cores and those observed in low-mass star-forming regions, where the line widths are dominated by thermal broadening, even in clustered environments (e.g. Kirk, Johnstone & Tafalla 2007; Walsh et al. 2007; Bourke et al. 2011).

In summary we highlight three regions where the gas is more turbulent (Fig. 9): (i) around IRS 3, especially in between IRS 1 and IRS 3 (see the  $C_2H$  and  $c-C_3H_2$  line widths in Fig. 9); (ii) north of MMA, near the red lobe; (iii) towards MMA. The turbulence enhancement around IRS 3 is easily explained by the expanding cavity, while in MMA (and north of it) could rather be due to the red-lobe of the outflow. On the other hand, we stress that towards MME and in between IRS 1 and IRS 3 some spectra show a double-velocity component [see e.g. the isolated hyperfine component in the  $N_2H^+(1-0)$  line towards MME in Fig. 6]. These are especially evident in the  $N_2H^+$ ,  $NH_3$  and  $NH_2D$  spectra, but the second component can be seen also in some spectra of  $C_2H$  and  $c-C_3H_2$  close to the cavity. Therefore, the large broadening above IRS 3 and in MME could just be due to the superposition of two unresolved velocity components.

Interestingly, for  $C_2H$  and  $N_2H^+$  the line broadening is relatively small close to the blue lobe of the outflow associated with IRS 1 and larger besides the red lobe, while the opposite seems to occur for the  $c-C_3H_2(2-1)$  line (top-middle panel in Fig. 9). This could indicate a selective influence of the flow on the different molecules in the surrounding material. However, we stress that the  $c-C_3H_2$  emission is very faint at the borders of the region plotted in Fig. 9, where the fit results are affected by large relative errors.

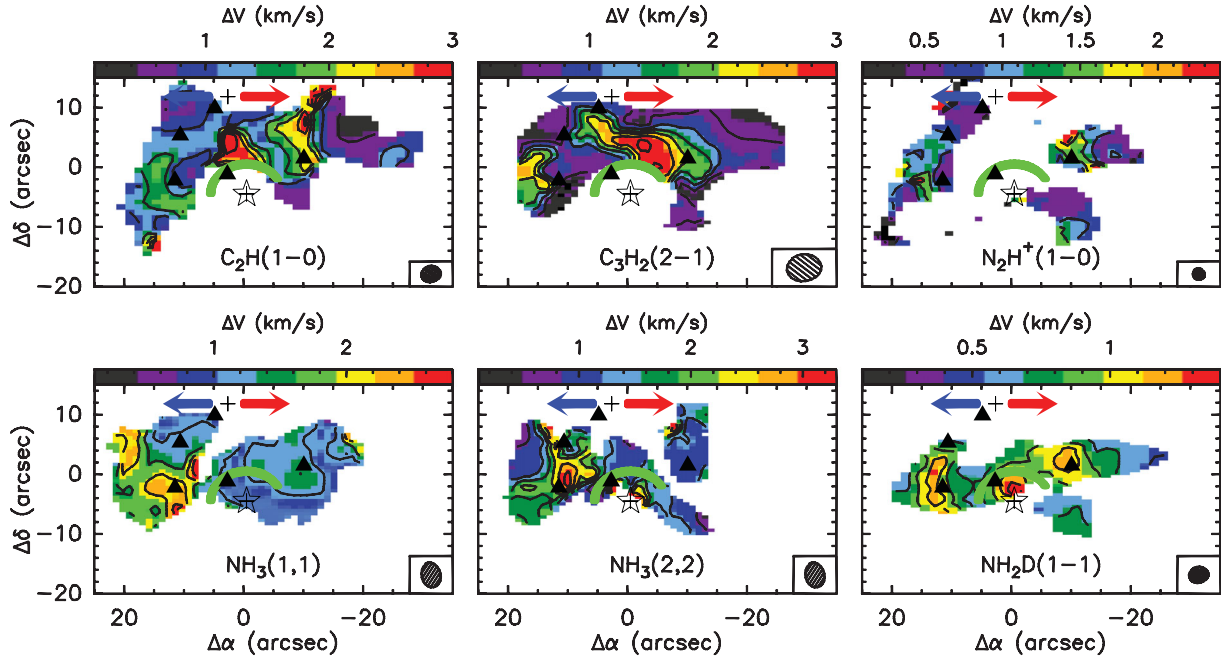


**Figure 9.** Same as Fig. 8 for the line widths. Contours are in steps of  $0.5 \text{ km s}^{-1}$  and range from  $0.5$  to  $3 \text{ km s}^{-1}$  for  $\text{C}_2\text{H}$ ,  $0.6$  to  $3.1 \text{ km s}^{-1}$  for  $c\text{-C}_3\text{H}_2$ ,  $0.4$  to  $2.4 \text{ km s}^{-1}$  for  $\text{N}_2\text{H}^+$ ,  $0.6$  to  $2.6 \text{ km s}^{-1}$  for  $\text{NH}_3(1,1)$ ,  $0.8$  to  $3.2 \text{ km s}^{-1}$  for  $\text{NH}_3(2,2)$ ,  $0.3$  to  $1.3 \text{ km s}^{-1}$  for  $\text{NH}_2\text{D}(1-1)$ .

### 3.3.3 Position–velocity plots

In order to further study the velocity field of the  $\text{NH}_3$  emission near IRS 3, we computed position–velocity plots for the  $\text{NH}_3(1,1)$  line in the east–west direction, and centred at offset  $0$  arcsec,  $-2$  arcsec with respect to the CARMA phase centre. The final plot is shown in panel ‘a’ of Fig. 10. The  $\text{NH}_3(1,1)$  emission in the position–velocity plot shows two main peaks, one corresponding to the eastern cloud and the other corresponding to the western cloud, and both peaks are linked through fainter emission, which shows an overall U-like structure. Such a feature resembles the shape predicted by the model of Arce et al. (2011) for an expanding bubble. In this model, an expanding shell would appear as a ring in the (position–velocity) plots (see their fig. 5), while we only see the blueshifted half of it. However, a U-like feature can be explained if the source driving the bubble is slightly displaced (behind the bubble) with respect to the surrounding molecular gas, so that we mainly see the gas that is moving towards us. In fact, the tails of the U-like feature are found, as expected, at approximately the systemic velocity. This suggests that IRS 3 may be pushing the surrounding dense material away (either through its winds/radiation or through the associated  $\text{H II}$  region), with an expansion velocity (difference between the ‘tip’ of the U-like feature and the ‘tails’) of about  $2 \text{ km s}^{-1}$  (see panel ‘a’ in Fig. 10). A similar expanding shell was recently found around an infrared-source at the centre of a region devoid of gas emission in the intermediate- to high-mass protocluster IRAS 05345+3157 (Fontani et al. 2012).

## 3.4 Physical parameters from 3 mm and 1.3 cm continuum emission

### 3.4.1 3 mm

We have identified five main condensations in the 3 mm continuum emission map (see Section 3.1). Their peak positions are given in

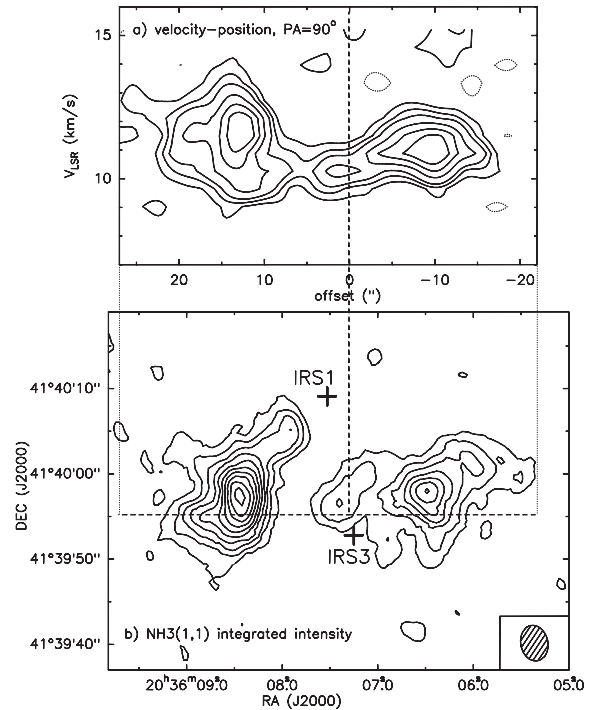


**Figure 10.** (a)  $\text{NH}_3(1,1)$  position–velocity plot centred at offset  $(0, -2)$  arcsec with respect to the CARMA phase centre and along a cut in the east–west direction. The  $\text{NH}_3(1,1)$  data cube was convolved with a beam of  $5 \times 2 \text{ arcsec}^2$  and  $\text{PA} = 0^\circ$  to increase signal-to-noise ratio. Contours are:  $-3, 3, 6, 9, 15, 21$  and  $27$  times  $0.001 \text{ Jy beam}^{-1}$ . (b)  $\text{NH}_3(1,1)$  integrated emission map (same contours as in Fig. 5) with the cut of the position–velocity plot of panel ‘a’ indicated by a dashed line. Contours start at 12 per cent of the peak intensity,  $224 \text{ Jy beam}^{-1} \text{ m s}^{-1}$ , and increase in steps of 10 per cent. The VLA synthesized beam is shown in the bottom-right corner.

**Table 3.** Peak position, angular and linear diameter, integrated flux density, mass, H<sub>2</sub> volume and column density of the 3 mm condensations detected with CARMA. The masses are computed for  $\beta = 2$ , and assuming the temperatures derived from ammonia. The H<sub>2</sub> volume and column densities are calculated assuming a spherical source with diameter equal to the deconvolved level at half-maximum.  $F_\nu$  has been obtained by integrating the continuum flux density inside the  $3\sigma$  contour level.

Core	Peak position		$T_k^a$ (K)	$F_\nu$ (mJy)	Diameter		$M_{\text{cont}}$ ( $M_\odot$ )	$n_{\text{H}_2}$ ( $\times 10^6 \text{ cm}^{-3}$ )	$N(\text{H}_2)$ ( $\times 10^{23} \text{ cm}^{-2}$ )
	RA(J2000) 20 <sup>h</sup> 36 <sup>m</sup>	Dec.(J2000)			$\theta_s$ (arcsec)	$D$ (pc)			
MMA	06 <sup>s</sup> :37	+41°39′59″.1	22 <sup>b</sup>	7.4	7.3	0.049	21	6.7	10.3
MMB	07 <sup>s</sup> :54	+41°39′55″.6	25	4.6	6.8	0.046	11	4.5	6.4
MMC	07 <sup>s</sup> :72	+41°40′07″.2	–	1.9	5.5	0.037	8 <sup>c</sup> ,4 <sup>d</sup>	6.2 <sup>c</sup> ,2.9 <sup>d</sup>	7.1 <sup>c</sup> ,3.3 <sup>d</sup>
MMD	08 <sup>s</sup> :23	+41°40′02″.0	14	3.7	6.3	0.043	17	8.7	11.4
MME	08 <sup>s</sup> :26	+41°39′54″.7	22	8.3	8.0	0.054	23	5.7	9.6

<sup>a</sup>Derived from  $T_{\text{rot}}$  as explained in Section 3.4.

<sup>b</sup>See Appendix A for the derivation of  $T_k$  from ammonia for this core.

<sup>c</sup> Assuming a temperature of 15 K.

<sup>d</sup> Assuming a temperature of 30 K.

Columns 2 and 3 of Table 3. We also list the angular ( $\theta$ ) and linear ( $D$ ) diameters (Columns 6 and 7 in Table 3) computed assuming the sources are Gaussians, and deconvolving the contour at half-maximum with a Gaussian beam with half power beam width (HPBW) corresponding to the geometric mean of the minor and major axes of the CARMA synthesized beam (see Table 1). Because the contours at half-maximum were blended, at the edge between two cores we decided to separate the emission arising from the different condensations identifying the peaks and considering the first unblended contour. The same criterion was applied to derive the integrated flux density,  $F_\nu$ , given in Column 5 of Table 3.

From  $F_\nu$ , we have computed the mass of the condensations under the assumptions that the dust millimetre-continuum emission is optically thin, and that the dust temperature equals the gas kinetic temperature. This latter hypothesis implies coupling between gas and dust, which is a reasonable assumption for H<sub>2</sub> volume densities above  $10^5 \text{ cm}^{-3}$ . Under these assumptions, the gas mass can be derived from the formula:

$$M = \frac{F_\nu d^2}{B_\nu(T)k_\nu}, \quad (1)$$

where  $d$  is the source distance,  $B_\nu(T)$  is the Planck function at dust temperature  $T$  and  $k_\nu$  is the dust opacity per unit dust mass. For this latter, we extrapolated the value at 230 GHz given by Kramer et al. (1998),  $k_{230} = 0.005 \text{ cm}^2 \text{ g}^{-1}$  (which assumes a gas-to-dust ratio of 100), through the power law  $k_\nu = k_{230}[\nu(\text{GHz})/230]^\beta$ . We have assumed  $\beta = 2$ , which is a typical value derived for dusty envelopes of massive (proto)stellar objects (e.g. Molinari et al. 2000; Hill, Thompson & Burton 2006). As gas temperature, we have taken the kinetic temperature obtained by extrapolating the rotation temperature derived from the ammonia (2,2)/(1,1) line ratio for each core (see Section 3.2.2 and Table 2) following the empirical approximation method described in Tafalla et al. (2004). The kinetic temperatures derived this way are listed in Column 4 of Table 3, and are in between 14 and 25 K, higher (a factor of 1.5–2) than the values measured typically in low-mass clustered starless cores (e.g. André et al. 2007; Foster et al. 2009) which are around 10–13 K. For MMC, undetected in NH<sub>3</sub> (2,2), we decided to give a range of masses computed in the temperature interval 15–30 K.

The resulting masses are listed in Column 8 of Table 3. All fragments have masses consistent with intermediate- to high-mass embedded objects. The most massive one is MME (23  $M_\odot$ ). By assuming spherical and homogeneous cores, we have derived the average H<sub>2</sub> volume and column densities. The average volume and

column densities (given in Columns 9 and 10 of Table 3) are of the order of  $10^{6-7} \text{ cm}^{-3}$  and  $10^{23-24} \text{ cm}^{-2}$ . Such high column densities are consistent with being the birthplaces of intermediate- and/or high-mass objects (e.g. Krumholz & McKee 2008).

### 3.4.2 1.3 cm

In Section 3.1 we showed that the centimetre emission is dominated by one single source associated with IRS 3 and extending towards the east. In addition, a secondary source near MMD was also identified. A 3.6 and 6 cm source associated with IRS 3 is already reported by Miralles et al. (1994) and Carral et al. (1999). However, from these two measurements only, and taking into account the uncertainties, the spectral index of the centimetre source associated with IRS 3 could not be well determined (e.g. Palau et al. 2007b). Our new measurement at 1.3 cm allows us to better constrain the spectral index of the source to  $0.1 \pm 0.2$  (Fig. 11). Such a spectral index is consistent with optically thin free-free emission favouring the interpretation that the centimetre emission comes from an H II region rather than a thermal radio jet (which typically have steeper spectral indices). We calculated the physical parameters of the ionized region at 1.3 cm assuming the emission is optically thin, and obtained an emission measure of  $3.4 \times 10^4 \text{ cm}^{-6} \text{ pc}$ , characteristic of UC H II

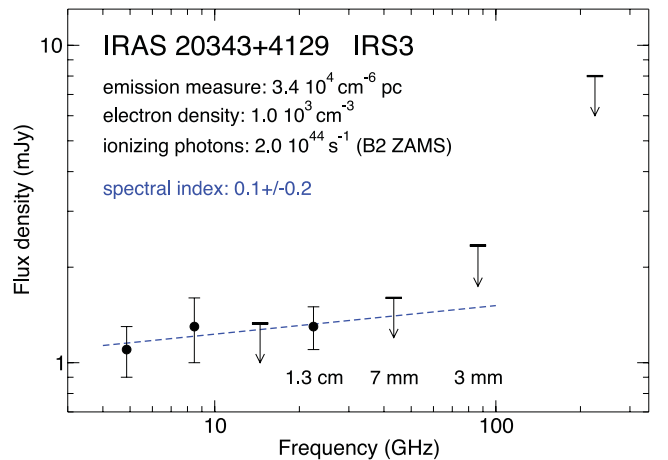


**Figure 11.** Spectral energy distribution of IRS 3 in the cm/mm range. The physical parameters have been derived assuming the emission at 1.3 cm comes from an optically thin H II region.

regions, and a flux of ionizing photons of  $2 \times 10^{44} \text{ s}^{-1}$ , consistent with the H II region being ionized by an early-type B2 star (Panagia 1973). Interestingly, the extension of such an UC H II region towards the east is similar (although larger in size) to the extension seen in [Ne II] emission by Campbell et al. (2008), and which is interpreted as due to the expansion of the ionized gas and disruption of the natal envelope. In this context, the secondary centimetre peak near MMD could be related as well to the expanding ionized gas. We estimated the possible contribution of free-free emission to the flux measured at 3 mm for MMB, and is of  $\sim 0.3 \text{ mJy}$  ( $4\sigma$  of 1.3 cm observations, and using the spectral index of 0.1), out of 4.6 mJy, or 6 per cent. Thus, thermal dust emission is the main contribution to the 3 mm continuum emission in MMB. Finally, we estimated an upper limit for the 3 mm emission associated with IRS 3 of 2.3 mJy, measured as the 3 mm flux density inside the  $4\sigma$  contour of the centimetre emission (Fig. 11), and we cannot rule out the possibility of the UC H II region being still associated with remnant natal dust, although a projection effect could be also possible.

## 4 DISCUSSION

### 4.1 Column densities of the PDR tracers $\text{C}_2\text{H}$ and $c\text{-C}_3\text{H}_2$

The two carbon-bearing species  $\text{C}_2\text{H}$  and  $c\text{-C}_3\text{H}_2$  are among the most abundant simple carbon-chain molecules detected in the interstellar medium, and are believed to be good tracers of PDRs (Lucas & Liszt 2000; Pety et al. 2005; Gerin et al. 2011).  $\text{C}_2\text{H}$  is formed either from photodissociation of acetylene ( $\text{C}_2\text{H}_2$ ) followed by dissociative recombination of  $\text{C}_2\text{H}_2^+$  (Mul & McGowan 1980) or through neutral-neutral reaction between C and  $\text{CH}_2$  in hot gas (Sakai et al. 2010).  $c\text{-C}_3\text{H}_2$  is believed to be formed by dissociative recombination of  $c\text{-C}_3\text{H}_3^+$ . Both species benefit from the presence of atomic carbon not locked in CO, and a good correlation between the two tracers has been found at the illuminated surface of the Horsehead nebula (Pety et al. 2005; Gerin et al. 2009), as well as in both diffuse and translucent clouds (Lucas & Liszt 2000; Gerin et al. 2011).

We have investigated the relation among the two species in I20343. For this purpose, we have extracted the spectra of  $\text{C}_2\text{H}$  (1–0) and  $c\text{-C}_3\text{H}_2$  (2–1) on a grid of spacing  $2.5 \times 2.5 \text{ arcsec}^2$  [roughly half of the CARMA synthesized beam at the frequency of the  $c\text{-C}_3\text{H}_2$  (2–1) transition], and fitted the spectra with Gaussian lines. Then, from the integrated intensity obtained from the fits, we have computed the column densities assuming that both lines are optically thin. This assumption is mandatory because the opacity of the lines cannot be directly measured [for the  $\text{C}_2\text{H}$  (1–0) line we observed only the main hyperfine component, and we do not have isotopologues for  $c\text{-C}_3\text{H}_2$ ]. However, given that the line profiles generally do not show effects due to high optical depths, we are confident that the assumption is reasonable. We used the general formula for optically thin transitions (compare to e.g. equation A.3 in Pillai et al. 2007):

$$N_{\text{tot}} = \frac{3h}{8\pi^3} \frac{Q(T_{\text{ex}})}{S\mu^2} \frac{W}{J_\nu(T_{\text{ex}}) - J_\nu(T_{\text{BG}})} e^{\left(\frac{E_J}{kT_{\text{ex}}}\right)} \quad (2)$$

where  $E_J$  and  $S$  are energy of the upper level and line strength, respectively;  $W$  is the integrated intensity of the line;  $Q(T_{\text{ex}})$  is the partition function at the temperature  $T_{\text{ex}}$ ;  $\nu$  is the line rest frequency;  $J_\nu(T_{\text{ex}})$  and  $J_\nu(T_{\text{BG}})$  are the equivalent Rayleigh–Jeans temperature at frequency  $\nu$  computed for the excitation and background temperature ( $T_{\text{BG}} \sim 2.7 \text{ K}$ ), respectively; and  $\mu$  is the molecule’s dipole moment (0.77 Debye for  $\text{C}_2\text{H}$  and 3.27 Debye for  $c\text{-C}_3\text{H}_2$ ).

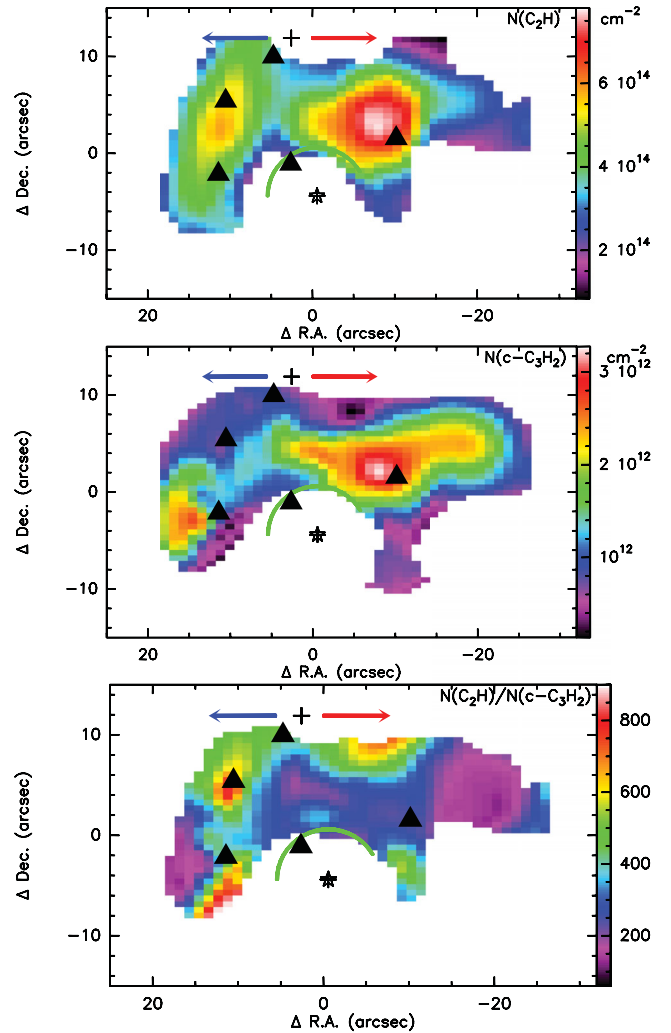


**Figure 12.** From top to bottom: column density map of  $\text{C}_2\text{H}$  and  $c\text{-C}_3\text{H}_2$ , and their ratio, derived from the CARMA observations. For the column density derivation of both species, an excitation temperature of 20 K has been adopted. The other symbols are the same as in Figs 8 and 9.

For  $\text{C}_2\text{H}$ , in equation (2),  $W$  has been obtained by multiplying the integrated emission of the hyperfine component observed for its relative intensity (0.416). As excitation temperature, we have assumed a reasonable value of 20 K based on the excitation temperatures computed for the other lines (see Table 2). The values of  $E_J$ ,  $S\mu^2$  and  $Q$  have been taken from the Cologne Database for Molecular Spectroscopy (CDMS;<sup>5</sup> Müller et al. 2001). For this latter, we have extrapolated the values tabulated to an excitation temperature of 20 K. For  $c\text{-C}_3\text{H}_2$ , the *ortho*/*para*-ratio is included in the partition function.

The results are shown in Fig. 12. The column density of  $\text{C}_2\text{H}$  is of the order of  $10^{14} \text{ cm}^{-2}$  across the cloud (Fig. 12, top panel), while that of  $c\text{-C}_3\text{H}_2$  is of the order of  $10^{12} \text{ cm}^{-2}$  (Fig. 12, middle panel). The  $\text{C}_2\text{H}$  column densities are generally larger than those found by Gerin et al. (2011), who measured column densities of  $10^{13} \text{ cm}^{-2}$ , while those of  $c\text{-C}_3\text{H}_2$  are more consistent. Their ratio is on average of the order of 200–400 (Fig. 12, bottom panel), i.e. one order of magnitude larger than the value 20–30 measured in translucent

<sup>5</sup> <http://www.astro.uni-koeln.de/cdms/>

clouds (Gerin et al. 2011), as well as in diffuse high latitude clouds (Lucas & Liszt 2000) and in the Horsehead nebula (Pety et al. 2005). On the other hand, the chemical models of PDRs in Gerin et al. (2011) seem to be more consistent with our observational results rather than with theirs, because the models predict total column densities consistent with our values for both species, and ratios of the order of 100 or even more (see their table 5). Interestingly, we find the largest ratios (around 400–800) close to the outflow lobes and to the east and west of the cavity walls, where the gas is probably less dense because of being most disrupted. Significant enhancement can be noticed also in the eastern clump, in between MMD and MME, where 1.3 cm emission is detected (see Section 3.1 and Fig. 2). This would strongly confirm that both molecules are produced in PDR regions, and that they are, perhaps, tracing a low-density envelope in which the dense cores detected in  $N_2H^+$  and  $NH_3$  are embedded.

#### 4.2 Chemical differentiation and nature of the 3 mm continuum cores

Studies of intermediate- and high-mass star-forming regions suggest that the relative abundance ratio  $NH_3$ -to- $N_2H^+$  is an evolutionary indicator for dense cores (e.g. Palau et al. 2007a; Fontani et al. 2012): cores with no signs of star formation typically have larger  $NH_3$ -to- $N_2H^+$  column density ratio than cores associated with active star formation. Also, Fontani et al. (2008) and Busquet et al. (2010) have measured that the deuterated fraction (i.e. the column density ratio of a deuterated species to that of the hydrogenated counterpart) of  $NH_3$  and  $N_2H^+$  is of the order of 0.1 in pre-protostellar core candidates, as high as in low-mass pre-stellar cores, while it is lower in more evolved objects. With this in mind, we have investigated the evolutionary stage of the millimetre cores in I20343 based on the column density ratios  $NH_3$ -to- $N_2H^+$  and  $NH_2D$ -to- $NH_3$ . From the line parameters derived in Section 3.2.2 (see Table 2) we have computed the total column densities of  $NH_3$ ,  $NH_2D$  and  $N_2H^+$  from equation (A1) of Caselli et al. (2002) because all lines are optically thick [except  $NH_2D$  (1–1) in MMD, but the opacity is well-constrained]. As for the other parameters, for a detailed discussion on the  $NH_3$  data of MMA, see Appendix A.

In Table 4 we report the column densities of  $NH_3$ ,  $NH_2D$  and  $N_2H^+$ , and the column density ratios  $NH_2D$ -to- $NH_3$  and  $NH_3$ -to- $N_2H^+$ . The  $NH_2D$ -to- $NH_3$  ratio is of the order of 0.1 (from  $\sim 0.07$  to 0.15), and does not change greatly from core to core. Such values are much larger than the cosmic D/H ratio, estimated to be  $\sim 10^{-5}$  (Linsky et al. 2006), and comparable to those measured towards low-mass pre-stellar cores (Roueff et al. 2005) and infrared dark clouds (Pillai et al. 2007). This implies that the deuteration in the cores of I20343 is as high as in colder and more quiescent environments,

despite the relatively higher gas temperature and turbulence, and confirms previous findings in other dense cores associated with intermediate- to high-mass star-forming regions (e.g. Busquet et al. 2010; Pillai et al. 2011). Interestingly, relatively high values are found also close to the UC H II region associated with IRS 3, in MMB and IRS3-SW. Because  $NH_2D$  is efficiently formed on dust grains, a strong UV radiation can heat the dust and cause  $NH_2D$  evaporation, thus increasing its abundance. On the other hand, a strong UV radiation could (at least partly) decrease the abundance of  $NH_3$ , due to its interaction with  $H^+$  to form  $NH_3^+$  (e.g. Fuente et al. 1993).

Concerning the  $NH_3$ -to- $N_2H^+$  ratio, we find the largest value in MME ( $\sim 80$ ). The enhancement of the  $NH_3$ -to- $N_2H^+$  ratio can be understood when freeze-out of species heavier than He becomes important (see e.g. Flower, Pineau Des Forêts & Walmsley 2006), so that it is expected to increase when the starless core gets closer to the onset of star formation. In this scenario, the fact that MME has the largest  $NH_3$ -to- $N_2H^+$  ratio suggests that this core could be close to the onset of gravitational collapse, i.e. MME could be a candidate massive pre-stellar core. However, Palau et al. (2007b) measured with the SMA a mass of only  $0.7 M_\odot$  from the 1.3 mm continuum, while we find  $23 M_\odot$ . This discrepancy likely comes from extended flux filtered out by the SMA, which means that the core is quite flat and not centrally peaked as expected for a pre-stellar core.

Based on the results of this work, we propose our final interpretation for the nature of each one of the 3 mm condensations:

(i) MMA is probably a protostar candidate. Although it does not show any embedded infrared source, its relatively high  $T_{rot}$ , large line broadening, and  $NH_2D$ -to- $NH_3$  lower than in other cores suggest that this condensation is evolved.

(ii) MME is likely a pre-stellar core, because it shows high  $NH_2D$ -to- $NH_3$  and  $NH_3$ -to- $N_2H^+$  ratios, is more quiescent than MMA and it does not appear fragmented into smaller condensations when observed at higher angular resolution (Palau et al. 2007b). Assuming a typical star formation efficiency of  $\sim 30$  per cent, the core, the mass of which is  $23 M_\odot$ , has the potential to form an intermediate- to high-mass object.

(iii) The nature of MMB, MMC and MMD is less clear. Due to the low  $NH_2D$ -to- $NH_3$  and  $NH_3$ -to- $N_2H^+$  ratios, MMD could be a protostellar object, consistent with clear hints of contraction motions seen in the  $NH_3$  (1,1) spectrum, while for MMB we found hints of expansion due to asymmetric emission in the two inner satellites (see Section 3.2.2). Certainly, all condensations are perturbed (MMB by the ionization front from IRS 3, MMC by IRS 1 and the outflow associated with it, MMD perhaps by a combination of both). Only higher sensitivity and angular resolution observations will allow us to better understand the nature of these cores.

**Table 4.** Total column densities of  $NH_3$ ,  $NH_2D$  and  $N_2H^+$  for the 3 mm continuum cores, except MMC, and the additional core IRS3-SW.

Core	$N(NH_3)$ ( $\times 10^{15} \text{ cm}^{-2}$ )	$N(N_2H^+)$ ( $\times 10^{13} \text{ cm}^{-2}$ )	$N(NH_2D)$ ( $\times 10^{14} \text{ cm}^{-2}$ )	$N(NH_2D)$ -to- $N(NH_3)$	$N(NH_3)$ -to- $N(N_2H^+)$
MMA	$>2.41^a$	7 (2)	2.2 (0.2)	$<0.09$	$>34$
MMB	2.3 (0.6)	–	2.6 (0.3)	0.11 (0.04)	–
MMD	3.1 (0.7)	13 (4)	2.1 (0.2)	0.068 (0.002)	24 (13)
MME	4.4 (0.7)	5.5 (0.7)	6.8 (0.7)	0.15 (0.04)	80 (23)
IRS3-SW	1.8 (0.4)	6 (3)	2.1 (0.2)	0.12 (0.04)	30 (22)

<sup>a</sup> See Appendix A for details on the derivation of the  $NH_3$  physical parameters.

### 4.3 Interaction of IRS 1 and IRS 3 with the dense gas: an expanding cavity

The most striking result of this work is the clear confirmation of a cavity opened by IRS 3 in the molecular surrounding gas, and a tight interaction between this cavity and the surrounding dense gas. We have found several evidence of this: (i) the morphology of all the molecular tracers, especially in  $C_2H$  and  $c-C_3H_2$ , delineates a cavity around IRS 3 and the 1.3 cm continuum map resolving the ionized gas perfectly matches the profile of the cavity; (ii) the  $NH_3$  integrated intensity (2,2)/(1,1) ratios are large near IRS 3; (iii) the line widths are also large near IRS 3, especially in  $C_2H$  and  $c-C_3H_2$ ; (iv) the position–velocity plot of  $NH_3$  shows a U-structure typical of an expanding shell; (v) in the MMB core we found hints of expansion in the  $NH_3$  (1,1) spectrum due to different intensity of the two inner satellites. These evidence of such an interaction are shown for the first time in this work.

If we put together all the results obtained, we speculate about a possible scenario that describes the star formation history in I20343: IRS 1 and IRS 3, both having bolometric luminosities of about  $1000 L_{\odot}$ , seem to come from the same natal cloud while being clearly in different evolutionary stages, which points towards different generations of (intermediate- to high-mass) star formation in I20343. In this context, IRS 3 could have induced the formation of IRS 1, as could be inducing star formation on the west (in MMA). On the other hand, in this bright-rimmed cloud the star formation probably has not been triggered by the UV radiation from the Cygnus OB2 association stars, because IRS 3, the massive star that formed first, is relatively distant from the bright rim, and the dense gas where we find the bulk of the current star formation activity is around IRS 3 and away from the bright rim. Therefore, the star formation seems to be dominated by IRS 3, which has been caught in the act of pushing away and disrupting its natal cloud.

## 5 SUMMARY AND CONCLUSIONS

The protocluster associated with the centre of I20343 is an excellent location where the interaction between evolved intermediate- and high-mass protostellar objects and dense (starless) cores can be studied. We have derived the physical and chemical properties of the dense gas by means of CARMA and VLA observations of the millimetre and centimetre continuum, and of several molecular tracers ( $C_2H$ ,  $c-C_3H_2$ ,  $NH_3$ ,  $NH_2D$ ,  $N_2H^+$ ). Below, we summarize the main results.

(i) Morphologically, the dense gas is distributed in a filament oriented east–west that passes in between IRS 1 and IRS 3, the two most massive and evolved objects. We resolve the dense gas into five millimetre continuum condensations. All of them show column densities consistent with potentially being the birthplace of intermediate- to high-mass objects, although the masses derived from continuum suggest that they can form intermediate-mass objects more likely.

(ii) We confirm the presence of an expanding cavity driven by IRS 3 demonstrated mainly by the shape of the emission in the two PDR tracers  $C_2H$  and  $c-C_3H_2$ , as well as by hints of expanding motions from both the position–velocity diagrams and the asymmetric intensity of the two inner satellites of the  $NH_3$  (1,1) line of the millimetre core closest to IRS 3 (MMB).

(iii) The non-thermal line widths across the filament indicate that the gas kinematics is dominated by turbulence, similarly to other

intermediate- and high-mass star-forming regions and different from low-mass dense starless cores.

(iv) The rotation and kinetic temperatures derived from ammonia are on average larger than those typically found in cores associated with low-mass star-forming regions, especially around the cavity walls. The most massive and extended millimetre core, MME, shows physical and chemical signatures of an intermediate- to high-mass pre-stellar core candidate.

(v) We have better constrained the spectral index of the radio-continuum emission associated with IRS 3, which turns out to be flat, and thus the ionized gas comes from a photoionized region from the B2 zero-age main sequence (ZAMS) star at the centre of IRS 3.

(vi) The column density ratio  $C_2H/c-C_3H_2$  is of the order of 200–400 across the source and is higher where the dense gas is getting disrupted.

(vii) The deuterated fraction  $NH_2D$ -to- $NH_3$  is of the order of 0.1 in all cores, as large as in low-mass pre-stellar cores and infrared dark clouds. We find high levels of deuteration also close to the cavity driven by IRS 3. We speculate that evaporation of  $NH_2D$  and  $NH_3$  destruction caused by the UV radiation field can influence this high deuteration.

These findings undoubtedly confirm a tight interaction in I20343 between the most massive and evolved objects and the dense surrounding starless cores in several respects (kinematics, temperature, chemical gradients), and suggest that IRS 3 could have induced the formation of IRS 1 and of the other gaseous condensations accumulated on the cavity walls. However, the large-scale morphology of the molecular tracers suggests that we are likely seeing only a limited portion of a very extended gaseous filament. Only a large pc-scale mosaic will allow us to fully trace the distribution of the dense gas in the region and delineate a complete view of the core population.

## ACKNOWLEDGMENTS

Support for CARMA construction was derived from the Gordon and Betty Moore Foundation, the Kenneth T. and Eileen L. Norris Foundation, the James S. McDonnell Foundation, the Associates of the California Institute of Technology, the University of Chicago, the states of California, Illinois, and Maryland, and the National Science Foundation. Ongoing CARMA development and operations are supported by the National Science Foundation under a cooperative agreement, and by the CARMA partner universities. We acknowledge support from the Owens Valley Radio Observatory, which is supported by the National Science Foundation through grant AST 05-40399. AP is grateful to Inma Sepúlveda for insightful discussions. AP is supported by the Spanish MICINN grant AYA2008-06189-C03 (co-funded with FEDER funds) and by a JAE-Doc CSIC fellowship co-funded with the European Social Fund under the programme ‘Junta para la Ampliación de Estudios’. GB is funded by an Italian Space Agency (ASI) fellowship under contract number I/005/07/01. We are grateful to the anonymous referee for his/her valuable comments and suggestions.

## REFERENCES

- André Ph., Belloche A., Motte F., Peretto N., 2007, *A&A*, 472, 519  
 Arce H. G., Borkin M. A., Goodman A. A., Pineda J. E., Beaumont C. N., 2011, *ApJ*, 742, 105  
 Beuther H., Schilke P., Menten K. M., Motte F., Sridharan T. K., Wyrowski F., 2002, *ApJ*, 566, 945

- Beuther H., Semenov D., Henning Th., Linz H., 2008, *ApJ*, 675, L33
- Bourke T. L., Myers P. C., Caselli P., Di Francesco J., Belloche A., Plume R., Wilner D. J., 2012, *ApJ*, 745, L117
- Briggs D. S., 1995, *BAAS*, 27, 1444
- Busquet G., Palau A., Estalella R., Girart J. M., Anglada G., Sepúlveda I., 2009, *A&A*, 506, 1183
- Busquet G., Palau A., Estalella R., Girart J. M., Sánchez-Monge Á., Viti S., Ho P. T. P., Zhang Q., 2010, *A&A*, 517, L6
- Campbell M. F. et al., 2008, *ApJ*, 673, 954
- Carral P., Kurtz S., Rodríguez L. F., Martí J., Lizano S., Osorio M., 1999, *Revista Mexicana Astron. Astrofísica*, 35, 97
- Caselli P., Walmsley C. M., Zucconi A., Tafalla M., Dore L., Myers P. C., 2002, *ApJ*, 565, 344
- Flower D. R., Pineau Des Forêts G., Walmsley C. M., 2006, *A&A*, 456, 215
- Fontani F., Caselli P., Bourke T. L., Cesaroni R., Brand J., 2008, *A&A*, 477, L45
- Fontani F., Zhang Q., Caselli P., Bourke T. L., 2009, *A&A*, 499, 233
- Fontani F., Caselli P., Zhang Q., Brand J., Busquet G., Palau A., 2012, preprint (arXiv:1203.3412)
- Foster J. B., Rosolowsky E. W., Kauffmann J., Pineda J. E., Borkin M. A., Caselli P., Myers P. C., Goodman A. A., 2009, *ApJ*, 696, 298
- Friesen R. K., Di Francesco J., Shirley Y. L., Myers P. C., 2009, *ApJ*, 697, 1457
- Fuente A., Martín-Pintado J., Cernicharo J., Bachiller R., 1993, *A&A*, 276, 473
- Gerin M., Goicoechea J. R., Pety J., Hily-Blant P., 2009, *A&A*, 494, 977
- Gerin M., Kaźmierczak M., Jastrzebska M., Falgarone E., Hily-Blant P., Godard B., de Luca M., 2011, *A&A*, 525, A116
- Hennebelle P., Commerçon B., Joos M., Klessen R. S., Krumholz M., Tan J. C., Teyssier R., 2011, *A&A*, 528, 72
- Hill T., Thompson M. A., Burton M. G., 2006, *MNRAS*, 368, 1223
- Ho P. T. P., Townes C. H., 1983, *ARA&A*, 21, 239
- Kirk H., Johnstone D., Tafalla M., 2007, *ApJ*, 668, 1042
- Kramer C., Kramer C., Alves J., Lada C., Lada E., Sievers A., Ungerechts H., Walmsley M., 1998, *A&A*, 329, L33
- Krumholz M. R., McKee C. F., 2008, *Nat*, 451, 1082
- Krumholz M. R., Klein R. I., McKee C. F., 2011, *ApJ*, 740, 74
- Kumar M. S. N., Bachiller R., Davis C. J., 2002, *ApJ*, 576, 313
- Lee H.-G., Koo B.-C., Park Y.-S., Ho P. T. P., 2002, *JKAS*, 35, 105
- Linsky J. L. et al., 2006, *ApJ*, 647, 1106
- Longmore S. N., Burton M. G., Barnes P. J., Wong T., Purcell C. R., Ott J., 2007, *MNRAS*, 379, 535
- Lucas R., Liszt H. S., 2000, *A&A*, 358, 1069
- Miralles M. P., Rodríguez L. F., Tapia M., Roth M., Persi P., Ferrari-toniolo M., Curiel S., 1994, *A&A*, 282, 547
- Molinari S., Brand J., Cesaroni R., Palla F., 2000, *A&A*, 355, 617
- Mul P. M., McGowan J. W., 1980, *ApJ*, 237, 749
- Müller H. S. P., Thorwirth S., Roth D. A., Winnewisser G., 2001, *A&A*, 370, L49
- Padovani M., Walmsley C. M., Tafalla M., Galli D., Müller H. S. P., 2009, *A&A*, 505, 1199
- Palau A., Estalella R., Girart J. M., Ho P. T. P., Zhang Q., Beuther H., 2007a, *A&A*, 465, 219
- Palau A., Estalella R., Ho P. T. P., Beuther H., Beltrán M. T., 2007b, *A&A*, 474, 911
- Palau A., Sánchez-Monge Á., Busquet G., Estalella R., Zhang Q., Ho P. T. P., Beltrán M. T., Beuther H., 2010, *A&A*, 510, A5
- Panagia N., 1973, *ApJ*, 78, 929
- Park Y.-S., 2001, *A&A*, 376, 348
- Peeters E., Hony S., Van Kerckhoven C., Tielens A. G. G. M., Allamandola L. J., Hudgins D. M., Bauschlicher C., 2002, *A&A*, 390, 1089
- Pety J., Teyssier D., Fossé D., Gerin M., Roueff E., Abergel A., Habart E., Cernicharo J., 2005, *A&A*, 435, 885
- Pillai T., Wyrowski F., Hatchell, Gibb J. A. G., Thompson M. A., 2007, *A&A*, 467, 207
- Pillai T., Kauffmann J., Wyrowski F., Hatchell J., Gibb A. G., Thompson M. A., 2011, *A&A*, 530, 118
- Purcell C. R. et al., 2009, *A&A*, 504, 139
- Roueff E., Lis D. C., van der Tak F. F. S., Gerin M., Goldsmith P. F., 2005, *A&A*, 438, 585
- Rygl K. L. J. et al., 2012, *A&A*, 539, A79
- Sakai N., Saruwatari O., Sakai T., Takano S., Yamamoto S., 2010, *A&A*, 512, 31
- Sridharan T. K., Beuther H., Schilke P., Menten K. M., Wyrowski F., 2002, *ApJ*, 566, 931
- Stutzki J., Winnewisser G., 1985, *A&A*, 144, 13
- Tafalla M., Myers P. C., Caselli P., Walmsley C. M., 2004, *A&A*, 416, 191
- Torrelles J. M., Verdes-Montenegro L., Ho P. T. P., Rodriguez L. F., Canto J., 1993, *ApJ*, 410, 202
- Walsh A. J., Myers P. C., Di Francesco J., Mohanty S., Bourke T. L., Gutermuth R., Wilner D., 2007, *ApJ*, 655, 958
- Zhang Q., Hunter T. R., Sridharan T. K., Ho P. T. P., 2002, *ApJ*, 566, 982

## APPENDIX A: ANALYSIS FOR THE CASE OF DIFFERENT $T_{\text{ex}}$ FOR THE MAIN AND THE INNER SATELLITE LINES OF $\text{NH}_3(1, 1)$

Let us assume that the line width of the magnetic hyperfine components of the  $\text{NH}_3(1, 1)$  inversion transition is large enough to make them unresolved, so that only the five electric hyperfine lines, i.e. one main line ('m'), two inner satellites ('is') and two outer satellites ('os'), are resolved. Assuming that the excitation temperature is  $T_{\text{ex}} \gg T_{\text{bg}}$ , the ratio of intensities of the main line to the inner satellite line is

$$\frac{T_{\text{MB}}(1, 1; \text{is})}{T_{\text{MB}}(1, 1; \text{m})} = \frac{T_{\text{ex}}(1, 1; \text{is})(1 - e^{-\tau_{\text{is}}})}{T_{\text{ex}}(1, 1; \text{m})(1 - e^{-\tau_{\text{m}}})} \quad (\text{A1})$$

The usual assumption is that we are observing a homogeneous isothermal region, so that both excitation temperatures,  $T_{\text{ex}}(1, 1; \text{is})$  and  $T_{\text{ex}}(1, 1; \text{m})$ , are equal, and that  $\tau_{\text{is}} = 0.28 \tau_{\text{m}}$ . In this case,

$$0.28 \leq \frac{T_{\text{MB}}(1, 1; \text{is})}{T_{\text{MB}}(1, 1; \text{m})} \leq 1. \quad (\text{A2})$$

The lower limit corresponds to the optically thin case, while the upper limit is the optically thick case.

In Section 3.2.2 we have shown  $\text{NH}_3(1, 1)$  spectra for each of the 3 mm continuum clumps. For the case of MMA, the intensity ratio of the inner satellites and the main line is  $0.23 \pm 0.05$ , lower than the optically thin limit, 0.28.

The assumption that the observed ratio is close to 0.28, and that the emission in MMA is optically thin, leads to inconsistent results. For an optical depth of the main line of  $\tau_{\text{m}} < 0.1$ , we obtain that  $T_{\text{ex}} > 230$  K, which is much higher than the kinetic temperature estimated from the intensities ratio  $T_{\text{MB}}(2, 2)/T_{\text{MB}}(1, 1)$  (see text),  $T_{\text{k}} = 22$  K. This result is improbable, since we expect the excitation temperature to be, in general, lower than the kinetic temperature.

The intensity of the  $(1, 1; \text{m})$  is close to the kinetic temperature, indicating that the optical depth of the main line is probably  $\tau_{\text{m}} \gg 1$ . The optical depth of the satellite, however, can be lower, so that both lines are tracing the emission of different layers of the region observed: the main line, the outer layer facing the observer; and the satellite line, a deeper layer of material (see Fig. A1). The easiest explanation of the anomalous ratio  $T_{\text{MB}}(1, 1; \text{is})/T_{\text{MB}}(1, 1; \text{m})$  is to assume that the region is not isothermal, and that the two layers at different physical depths, have different temperatures. So, the two excitation temperatures,  $T_{\text{ex}}(1, 1; \text{is})$  and  $T_{\text{ex}}(1, 1; \text{m})$ , are not equal. Thus,

$$\frac{T_{\text{ex}}(1, 1; \text{is})}{T_{\text{ex}}(1, 1; \text{m})} \frac{1 - e^{-\tau_{\text{is}}}}{1 - e^{-\tau_{\text{m}}}} = \frac{T_{\text{MB}}(1, 1; \text{is})}{T_{\text{MB}}(1, 1; \text{m})} = 0.23. \quad (\text{A3})$$

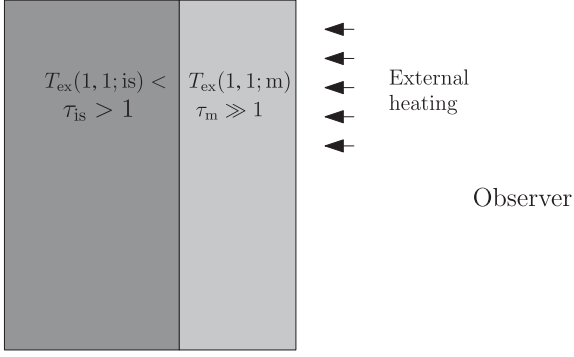


**Figure A1.** Geometry of MMA.

Assuming that  $T_{\text{ex}}(1, 1; m)$  is lower than  $T_k$ ,

$$T_{\text{MB}}(1, 1; m) \leq T_k(1 - e^{-\tau_m}), \quad (\text{A4})$$

giving that the optical depth of the main line must be  $\tau_m \geq 3.1$ . Thus, taking into account that  $\tau_{\text{is}} = 0.28 \tau_m$ , we obtain

$$0.61 \leq \frac{1 - e^{-\tau_{\text{is}}}}{1 - e^{-\tau_m}} \leq 1, \quad (\text{A5})$$

resulting in

$$0.23 \leq \frac{T_{\text{ex}}(1, 1; \text{is})}{T_{\text{ex}}(1, 1; m)} \leq 0.38. \quad (\text{A6})$$

The result is that the deeper layer traced by the satellite line is colder than the outer layer traced by the main line. If we assume that the kinetic temperature of MMA, obtained from the ratio  $T_{\text{MB}}(2, 2)/T_{\text{MB}}(1, 1)$ , is tracing the outer layer, the outer layer temperature is 22 K, while the inner layer temperature is between 5 and 8 K. The higher temperature of the outer layer is indicative of external heating, as discussed in the text.

This paper has been typeset from a  $\text{\TeX}/\text{\LaTeX}$  file prepared by the author.